nature communications

Article

https://doi.org/10.1038/s41467-024-54376-x

Astrocytic inhibition of lateral septal neurons promotes diverse stress responses

Received: 18 April 2024

Accepted: 5 November 2024

Published online: 21 November 2024

Check for updates

Kain Seo[1,2,8], Sanghyun Won[1,2,8], Hee-Yoon Lee[3,8], Yeonju Sin[1], Sangho Lee[1,2], Hyejin Park[4], Yong Geon Kim[1], Seo Young Yang[1], Dong-Jae Kim[4], Kyoungho Suk[5], Ja Wook Koo[6], Myungin Baek[1], Se-Young Choi[3] ✉ & Hyosang Lee[1,2,7] ✉

Inhibitory neuronal circuits within the lateral septum (LS) play a key role in regulating mood and stress responses. Even though glial cells can modulate these circuits, the impact of astrocytes on LS neural circuits and their functional interactions remains largely unexplored. Here, we demonstrate that astrocytes exhibit increased intracellular Ca^{2+} levels in response to aversive sensory and social stimuli in both male and female mice. This astrocytic Ca^{2+} elevation inhibits neighboring LS neurons by reducing excitatory synaptic transmissions through A_1R-mediated signaling in both the dorsal (LSd) and intermediate LS (LSi) and enhancing inhibitory synaptic transmission via A_{2A}R-mediated signaling in the LSi. At the same time, astrocytes reduce inhibitory tone on distant LS neurons. In the LSd, astrocytes promote social avoidance and anxiety, as well as increased heart rate in socially stressed male mice. In contrast, astrocytes in the LSi contribute to elevated heart rate and heightened blood corticosterone levels in unstressed male mice. These results suggest that the dynamic interactions between astrocytes and neurons within the LS modulate physiological and behavioral responses to stressful experiences.

Experiencing a harmful stimulus or engaging in an aggressive encounter disrupts ongoing neural activities in the brain, affecting the internal state and body homeostasis[1]. Prolonged exposure to stressors can lead to adverse emotional effects and pathological conditions such as anxiety disorders, social isolation, and depression[2–4]. The lateral septum (LS) is a forebrain region involved in stress responses and anxiety[5–8], as well as fear, sociability, feeding, and spatial memory[9–13]. Principally composed of GABAergic neurons, LS neurons respond to diverse aversive and stressful stimuli[14–17]. The LS receives strong synaptic inputs from the hippocampus and establishes both unidirectional and bidirectional connections with the prefrontal cortex, hypothalamus, bed nucleus of the stria terminalis, nucleus accumbens, and amygdala[5,18]. Cortical and subcortical input patterns show distinct spatial distributions across the LS subregions[18–20]. These innervation patterns and associated neural pathways may support functional disparities within the LS, suggesting spatially-restricted functions[21]. LS neurons not only project to downstream brain regions but also send collateral inhibitory projections to other neurons within the LS to form

[1]Department of Brain Sciences, Daegu Gyeongbuk Institute of Science & Technology (DGIST), Daegu, Republic of Korea. [2]Convergence Research Advanced Centre for Olfaction, Daegu Gyeongbuk Institute of Science & Technology (DGIST), Daegu, Republic of Korea. [3]Department of Physiology and Neuroscience, Dental Research Institute, Seoul National University School of Dentistry, Seoul, Republic of Korea. [4]Laboratory Animal Resource Center, Daegu Gyeongbuk Institute of Science & Technology (DGIST), Daegu, Republic of Korea. [5]Department of Pharmacology, School of Medicine, Brain Science and Engineering Institute, Kyungpook National University, Daegu, Republic of Korea. [6]Emotion, Cognition and Behavior Research Group, Korea Brain Research Institute (KBRI), Daegu, Republic of Korea. [7]Korea Brain Research Institute (KBRI), Daegu, Republic of Korea. [8]These authors contributed equally: Kain Seo, Sanghyun Won, Hee-Yoon Lee. ✉e-mail: sychoi@snu.ac.kr; hyosang22@dgist.ac.kr

local circuits[22,23]. These local circuits may process diverse presynaptic inputs to drive functional outcomes in the LS[24–26]. Advanced molecular genetic techniques have identified molecularly defined, discrete neuronal populations or ensembles within the LS. For example, a subset of LS neurons expressing corticotropin-releasing hormone receptor 2 (CRHR2) promotes stress and fear responses[6,15]. Neurotensin (NTS)-expressing neurons, which partially overlap with CRHR2$^+$ neurons, mediate chronic stress-induced social deficits[16]. In contrast, neurons expressing somatostatin (SST) play a role in suppressing stress-induced social avoidance and anxiety, while dopamine receptor D3-expressing neurons alleviate social deficits following early life stress[11,27,28]. Interestingly, some of these functionally distinct neuronal populations are activated by similar aversive stimuli. Further investigations into circumscribed neuronal circuits within the LS and the intricate interactions among those molecularly defined neuronal populations are necessary to understand the functional and physiological roles of the LS.

However, how non-neuronal cells like astrocytes contribute to the diverse functions in the LS remains unknown. Astrocytes modulate local neural circuits by influencing extracellular ionic composition, neurotransmitter levels, and the release of gliotransmitters in the perisynaptic area[29–31]. Astrocytes also contribute to processing stress and affective responses. For instance, astrocytes in the lateral habenula induce burst firing of neighboring neurons, thereby promoting depressive-like behaviors[32]. Astrocytic oxytocin receptors in the lateral part of the central nucleus of the amygdala (CeA) enhance GABAergic inputs to neurons in the medial CeA and increase anxiolytic behaviors[33]. We hypothesize that LS astrocytes, together with neurons, regulate responses to aversive and threatening stimuli and correlated stress responses and affective behaviors.

Here, we demonstrate that LS astrocytes elevate intracellular Ca^{2+} levels in response to aversive and stressful stimuli in vivo. This increase in astrocytic Ca^{2+} suppresses nearby LS neurons by reducing excitatory synaptic transmission via the activation of neuronal A_1 adenosine receptors in both the dorsal (LSd) and intermediate (LSi) regions. Concurrently, it enhances inhibitory synaptic transmission in the LSi through the activation of neuronal A_{2A} adenosine receptors. Furthermore, we find that LSd astrocytes promote social avoidance, anxiety-like behaviors, and increased heart rate in mice previously exposed to social defeat stress. In contrast, LSi astrocytes drive physiological stress responses in unstressed mice, including increased heart rate and elevated blood corticosterone levels. These findings suggest that astrocytes modulate neuronal activity in the LS and influence both physiological and behavioral responses to stress.

Results

LS astrocytes respond to aversive sensory and social stimuli in vivo

We delineated the distribution of astrocytes within the LS using immunofluorescent staining with two antibodies targeting the astrocyte-specific markers, S100β and glial fibrillary acidic protein (GFAP) (Supplementary Fig. 1a, b). S100β$^+$ cells were evenly distributed throughout the LS, but GFAP$^+$ cells were relatively more concentrated in the dorsal LS, although low-level expression was also seen in the rest of the LS.

Using fiber photometry, we then examined the intracellular Ca^{2+} levels of LS astrocytes (Fig. 1a). An adeno-associated virus (AAV) expressing the hgfaABC1D promoter-driven genetic Ca^{2+} indicator GCaMP6f was injected into the LS, and a fiber optic cannula was installed above the virus-injected region for recording purposes. Histological analysis utilizing the specific markers for astrocytes (GFAP) and neurons (NeuN) confirmed the selective expression of GCaMP6f in LS astrocytes (Fig. 1b and Supplementary Fig. 1c).

To systematically evaluate the responsiveness of LS astrocytes, we obtained fiber photometric Ca^{2+} recordings throughout the LS, mainly between bregma 0.62 and 0.02 mm (Supplementary Fig. 1g). Histological analysis of cannula damage enabled the classification of lateral septum placements into dorsal, intermediate, and ventral (LSv) according to the Mouse Brain Atlas (Supplementary Fig. 1g)[34]. Astrocytes in the LSd displayed a Ca^{2+} transient in response to an unexpected external movement toward a GCaMP6f-expressing mouse (Fig. 1c). In addition, LSd astrocytes responded to a visual stimulus that mimicked the approach of an airborne predator (Fig. 1d and Supplementary Movie 1). However, they did not respond to a neutral visual stimulus, a slow-moving grating, suggesting selective responsiveness to threatening stimuli (Fig. 1e). LSd astrocytes also responded to an electric shock delivered to the paw (Fig. 1f).

LSd astrocytes remained unresponsive to aversive stimuli produced by other modalities, including startling noise, fox urine (trimethylthiazoline), or bitter taste stimulus (denatonium benzoate), as well as rewarding stimuli such as a sucrose solution for water-deprived mice or food pellets for food-restricted mice (Supplementary Fig. 2a–e). Using the resident intruder paradigm, we investigated whether LSd astrocytes from a GCaMP6f-expressing male mouse exhibited changes in Ca^{2+} levels while interacting with an intruder. LSd astrocytes showed no Ca^{2+} changes during the appetitive phase of social interactions, including approach, investigation, or mounting, toward either a male or female intruder (Fig. 1g, h, and Supplementary Fig. 2f). Conversely, a rapid Ca^{2+} elevation was detected when a GCaMP6f-expressing male mouse was attacked by a CD-1 or C57BL/6 male aggressor (Fig. 1i, Supplementary Fig. 2g, and Supplementary Movie 2).

We then examined astrocytic responses to stressful experiences. We discovered that intracellular Ca^{2+} levels in LSd astrocytes did not change during tail suspension or restraint stress (Supplementary Fig. 2i, k). Interestingly, peak values did increase during tail suspension with concomitant signs of struggle (Supplementary Fig. 2i) or upon release from restraint (Supplementary Fig. 2l), consistent with previous findings regarding NTS$^+$ LS neuronal properties[17]. Wheel-running during the rotarod test did not trigger any alterations in astrocytic Ca^{2+} levels, indicating that astrocytic responses to aversive stimuli are not a consequence of heightened locomotion (Supplementary Fig. 2h). Altogether, LSd astrocytes selectively responded to a subset of dangerous, frightening, and stressful stimuli. They remained unresponsive to neutral and rewarding stimuli, as well as during the appetitive phase of social interaction.

Astrocytes in the LSi and LSv of male mice exhibited similar responses to aversive visual, somatosensory, and social stimuli (Supplementary Fig. 3a, b). However, unlike LSd astrocytes, LSi and LSv astrocytes exhibited small but significant increases in average Ca^{2+} levels during tail suspension and restraint stress (Supplementary Fig. 3a, b). In addition, LSi astrocytes displayed a significant increase in Ca^{2+} in response to a startling acoustic stimulus (Supplementary Fig. 3a). In female mice, Ca^{2+} responses of LSi astrocytes to aversive stimuli were similar to those observed in male mice, except in response to acoustic stimulation and restraint stress (Supplementary Fig. 3c). Detailed analysis of astrocytic responsiveness along the anteroposterior LS at bregma 0.62-0.5, 0.38-0.26, and 0.14-0.02 mm revealed an overall functional homogeneity of LS astrocytes in response to external stimuli, regardless of their subregional localization (Supplementary Fig. 3d–f). Taken together, these results suggest that LS astrocytes selectively respond to stimuli with strong negative valence.

Astrocytic responses to aversive stimuli require hippocampal inputs to the LS

To elucidate the mechanism driving Ca^{2+} responses in LS astrocytes after exposure to aversive stimuli, we predicted that neuronal inputs to the LS drive astrocyte responses. We visualized brain regions projecting to the LS using a retrograde AAV expressing hEF1α promoter-

https://doi.org/10.1038/s41467-024-54376-x

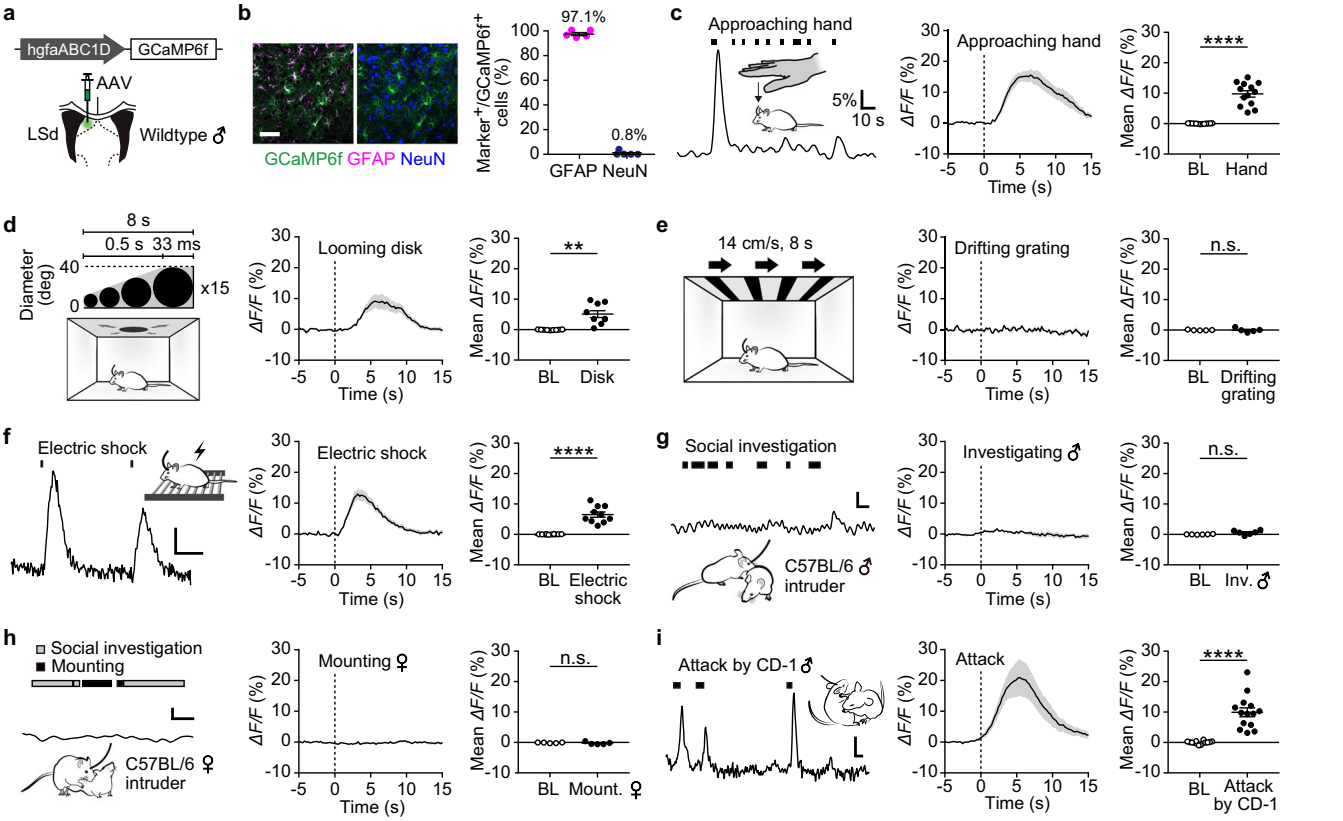

Fig. 1 | LS astrocytes respond to specific aversive sensory and social stimuli in vivo. An AAV expressing GCaMP6f under the control of the hgfaABC1D promoter was injected into the LS of wildtype mice resulting in the selective expression of GCaMP6f (*green*) in GFAP$^+$ astrocytes (*magenta*) but not in NeuN$^+$ neurons (*blue*) (**a**). Quantification of overlap obtained from 3 sections per mouse, across 5 mice (**b**). Intracellular Ca^{2+} levels in LSd astrocytes in response to various stimuli: an approaching hand (**c**), looming disk (**d**), drifting grating (**e**), electric shock (**f**), investigation of a male intruder (**g**), investigation and mounting of a female intruder (**h**), and attack by a CD-1 male intruder (**i**). In each set of panels, the first panel includes a representative Ca^{2+} trace (**c**, **f**–**i**) or a stimulus protocol (**d**, **e**). The second panel displays an averaged Ca^{2+} trace with the stimulus applied at 0 s, indicated by a vertical dotted line. The third panel shows the mean *ΔF/F* at baseline (*BL*, *open circles*) and after the stimulus (*filled circles*). Scale bar, 50 µm. The number of samples and the associated statistical details are listed in Supplementary Data 1. Source data are available in the Source Data file. $^{**}p < 0.01$, $^{****}p < 0.0001$, n.s., not significant. The data are presented as the mean ± SEM.

driven mCherry injected into the LSd (Supplementary Fig. 4a, b). Using the mCherry fluorescence patterns and the regions' reported roles in stress responses, we focused on the hippocampus (HPC), infralimbic cortex (IL), and lateral hypothalamic area (LHA) for further analysis[35–37].

Next, we inhibited neurons in candidate upstream regions using AAV to bilaterally express the Gi-linked chemogenetic effector, hM4Di-mCherry, and administering the agonist, clozapine-N-oxide (CNO) intraperitoneally (i.p.) (Fig. 2a, b). Silencing excitatory neurons in the dorsal hippocampus significantly reduced the amplitude of Ca^{2+} transients in LSd astrocytes elicited by our tested aversive stimuli, indicating that the hippocampal inputs contribute to astrocytic responses to these stimuli (Fig. 2c–h). The remaining Ca^{2+} responses suggest that additional mechanisms participate in generating astrocytic Ca^{2+} responses. However, silencing IL or LHA did not alter the Ca^{2+} responses of LS astrocytes, suggesting that these regions are dispensable for astrocytic responses in these stress responses, if at all necessary (Supplementary Fig. 4c–i).

To determine whether activation of hippocampal neurons can evoke Ca^{2+} transients in LS astrocytes, we expressed the optogenetic activator ChrimsonR in dorsal CA1 neurons (Fig. 2i, j)[38]. Photostimulation of ChrimsonR-expressing cell bodies in the hippocampus using red light at 635 nm increased Ca^{2+} levels in LS astrocytes (Fig. 2k, l). The astrocytic response was also triggered by photostimulation of ChrimsonR-expressing nerve terminals in the LS (Fig. 2m, n). Interestingly, a short delay was observed between photostimulation of hippocampal neuronal cell bodies or their terminals in the lateral septum (LS) and the subsequent increase in astrocytic Ca^{2+} levels, resembling the latency of astrocytic responses to aversive stimuli (Fig. 2k, l and Fig. 1). This delay may not reflect signaling through local neurons, as Ca^{2+} elevations in astrocytes triggered by an approaching hand and social defeat remained unaffected by the chemogenetic silencing of LS neurons using hM4Di (Supplementary Fig. 4j–l). Collectively, these results indicate that the hippocampus contributes to increasing Ca^{2+} levels in LS astrocytes.

LSd and LSi astrocytes inhibit neighboring neurons by activating neuronal adenosine receptors

To investigate the influence of elevated astrocytic Ca^{2+} levels on neuronal activity in the LS, we expressed the Gq-linked chemogenetic effector, hM3Dq, in either LSd or LSi astrocytes using an adeno-associated virus (AAV) and recorded LS neurons in septal slices (Fig. 3a, b). Histological analysis confirmed the predominant expression of mCherry and hM3Dq in their respective target cell types (Supplementary Fig. 1d, e). We demonstrated that manipulating astrocytes in the LSd and LSi using hM3Dq was insufficient to alter the intrinsic properties of LS neurons surrounded by hM3Dq-expressing astrocytes, such as the action potential firing rate, resting membrane potential, or input resistance (Supplementary Fig. 5a, b). However, hM3Dq-mediated manipulation of LSd astrocytes decreased the frequency of sEPSCs in those neurons, with no observable effect on sIPSCs (Fig. 3c, d). In contrast, the same manipulation of LSi astrocytes not only reduced the frequency of sEPSCs but also increased the

https://doi.org/10.1038/s41467-024-54376-x

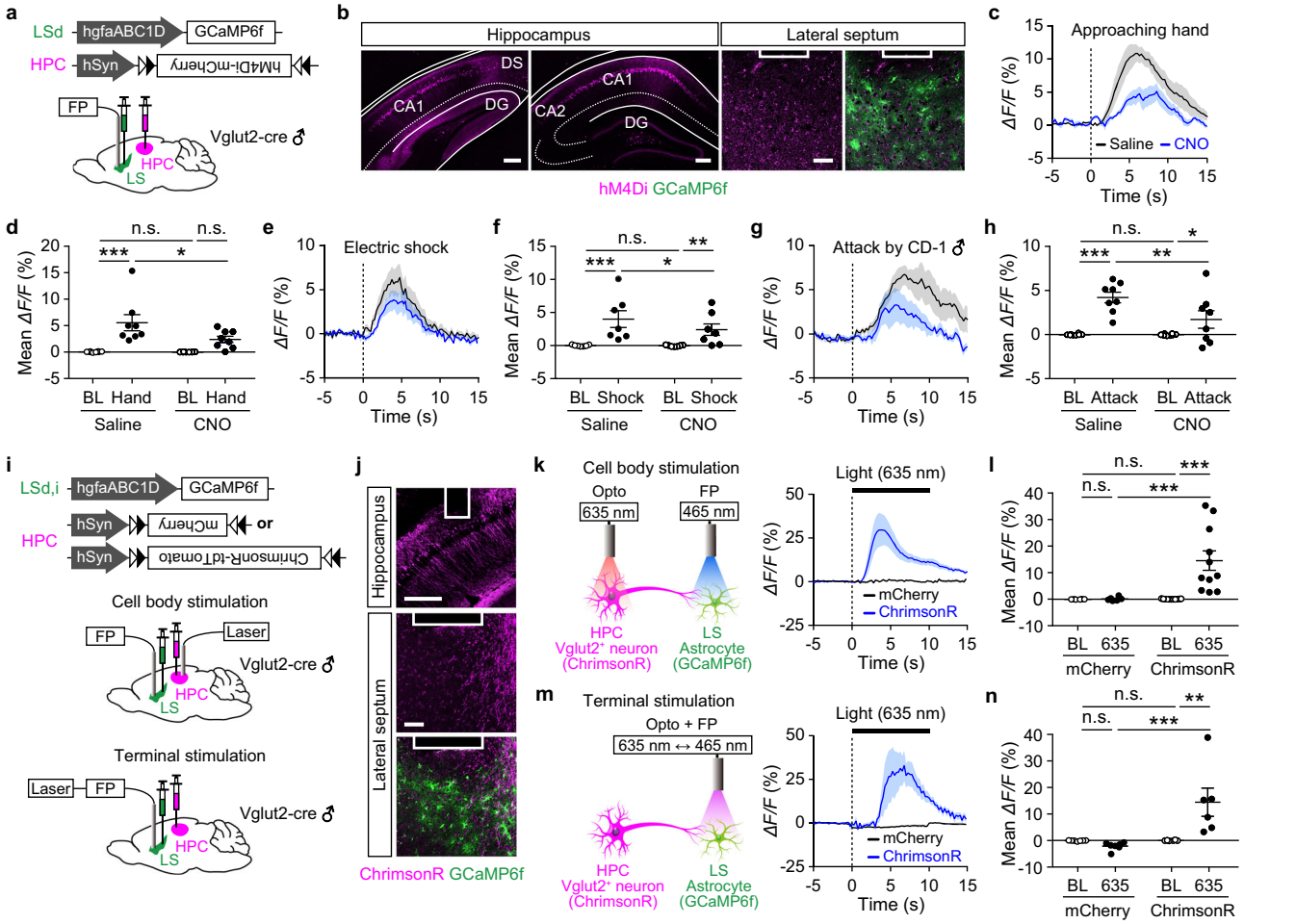

Fig. 2 | Hippocampal inputs to the LS are required for Ca^{2+} responses in LS astrocytes. Fiber photometric recording (*FP*) of LS astrocytes in Vglut2-cre mice expressing cre-dependent hM4Di-mCherry in the hippocampus (*HPC*) and GCaMP6f in LS astrocytes (**a**). The native fluorescence of hM4Di-mCherry in neuronal cell bodies in the hippocampus and their nerve terminals in the LS (*magenta*) and that of GCaMP6f in LS astrocytes (*green*). The experiment was repeated independently 8 times. **b** The white box in the images indicates cannula damage. Averaged Ca^{2+} traces and the mean *ΔF/F* of LS astrocytes elicited by an approaching hand (**c**, **d**), electric shock (**e**, **f**), or attack by a CD-1 male (**g**, **h**) at baseline (*BL*) and during-after the application of the indicated stimulus. Saline or CNO was administered 30 min before the onset of the stimulus at 0 s. Fiber photometric recordings of Vglut2-cre mice expressing cre-dependent mCherry or ChrimsonR-tdTomato (*ChrimsonR*) in the hippocampus and GCaMP6f in LS astrocytes (**i**). ChrimsonR expression in neuronal cell bodies in the hippocampus and in their nerve terminals in the LS (*magenta*) and GCaMP6f expression in LS astrocytes (*green*). The experiment was repeated independently 11 times. (**j**). The white box in the images indicates cannula damage. An averaged Ca^{2+} trace and the mean *ΔF/F* of LS astrocytes before (*BL*) and during photostimulation of the hippocampal cell bodies (**k**, **l**) or nerve terminals in the LS (**m**, **n**) with red light at 635 nm starting at 0 s. Scale bars, 200 μm (HPC) and 50 μm (LS). The number of samples and the associated statistical details are listed in Supplementary Data 1. Source data are available in the Source Data file. $^{*}p < 0.05$, $^{**}p < 0.01$, $^{***}p < 0.001$, n.s., not significant. The data are presented as the mean ± SEM.

frequency of sIPSCs in surrounding neurons (Fig. 3e, f). In addition, the amplitudes of sEPSCs and sIPSCs in LSi neurons increased following CNO treatment of LS slices containing LSi astrocytes expressing hM3Dq, compared to the untreated CNO group (Fig. 3e, f). However, these increases were not statistically significant compared to the mCherry-expressing group (Fig. 3e, f). Interestingly, a subset of neurons in the LSi area with low or absent hM3Dq expression showed a decrease in both the amplitude and frequency of sIPSCs following astrocytic manipulation (Supplementary Fig. 6a–d). These findings suggest that astrocytes exert inhibitory effects on nearby LS neurons, while simultaneously reducing inhibitory influences on distant neurons.

Extracellular adenosine from astrocytes modulates sIPSC and sEPSC frequency[39–42]. Thus, we predicted that adenosine receptors regulate LS astrocytic responses. The adenosine A_1 receptor (ADORA1 or A_1R) antagonist DPCPX reversed the decreased sEPSC frequency in both LSd and LSi neurons, while the adenosine A_{2A} receptor (ADORA2 or $A_{2A}R$) antagonist KW6002 reversed the increased sIPSC frequency in LSi neurons (Fig. 4a–d). Consistent with these findings, the A_1R agonist CCPA decreased the frequency of sEPSCs in both LSd and LSi neurons (Supplementary Fig. 7a, b). In addition, the $A_{2A}R$ agonist CGS21680 increased the frequency of sIPSCs, specifically in LSi neurons (Supplementary Fig. 7c, d). mEPSCs and sEPSCs exhibited similar patterns in both the LSd and LSi (Fig. 3c, e, and Supplementary Fig. 7e, f). Astrocyte manipulations in the LSi did not affect the mIPSC frequency in the LSi, in contrast to the impact of these manipulations on sIPSC frequency (Supplementary Fig. 7g). This result suggests that the astrocyte-mediated increases in sIPSCs depend on presynaptic mechanisms. Finally, astrocyte manipulations did not alter eEPSCs or eIPSCs, or affect the paired-pulse ratio (PPR) in LSd neurons (Supplementary Fig. 5c–e). In contrast, manipulating astrocytes with hM3Dq increased both eEPSCs and eIPSCs in LSi neurons (Supplementary Fig. 5f). Since the PPR in the LSi was unaltered, we conclude that these evoked responses do not arise from changes in the probability of neurotransmitter release (Supplementary Fig. 5g, h). Together, these results suggest that LS astrocytes exert an inhibitory influence on LS

https://doi.org/10.1038/s41467-024-54376-x

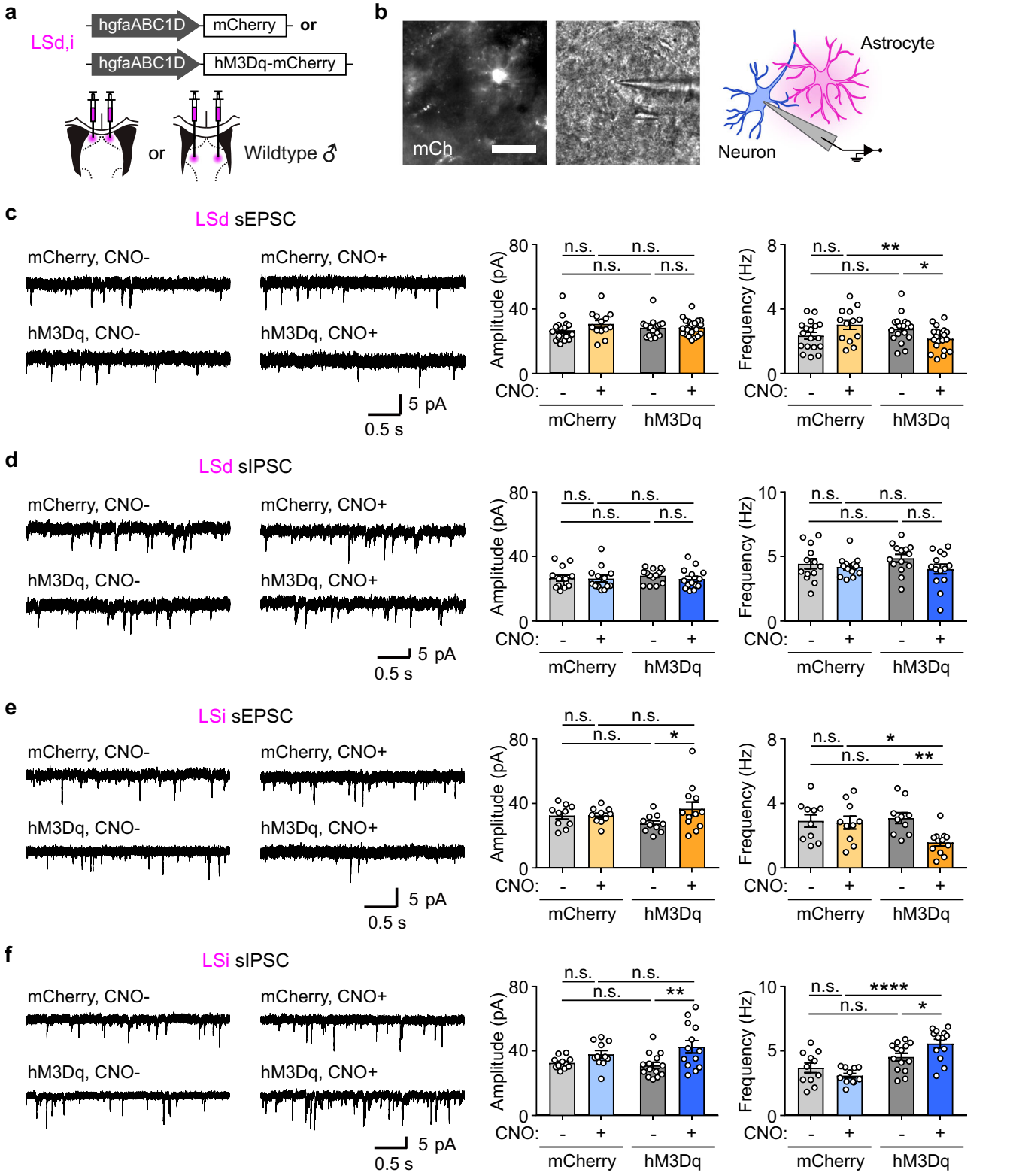

Fig. 3 | Astrocytes exert inhibitory influences on neighboring neurons by regulating synaptic transmissions in the LS. Voltage-clamp recordings of LS neurons in acute septal slices expressing mCherry or hM3Dq in LS astrocytes. Schematic showing AAV injection into either LSd or LSi (**a**). A brain slice displaying an astrocyte expressing mCherry alongside a neuron recorded using a patch pipette. The experiment was repeated independently 20 times (**b**). Representative traces and quantification of the amplitude and frequency of sEPSCs and sIPSCs recorded from neighboring LSd neurons (**c**, **d**) and LSi neurons (**e**, **f**). Scale bars, 50 μm. The number of samples and the associated statistical details are listed in Supplementary Data 1. Source data are available in the Source Data file. *$p < 0.05$, **$p < 0.01$, ****$p < 0.0001$, n.s., not significant. The data are presented as the mean ± SEM.

https://doi.org/10.1038/s41467-024-54376-x

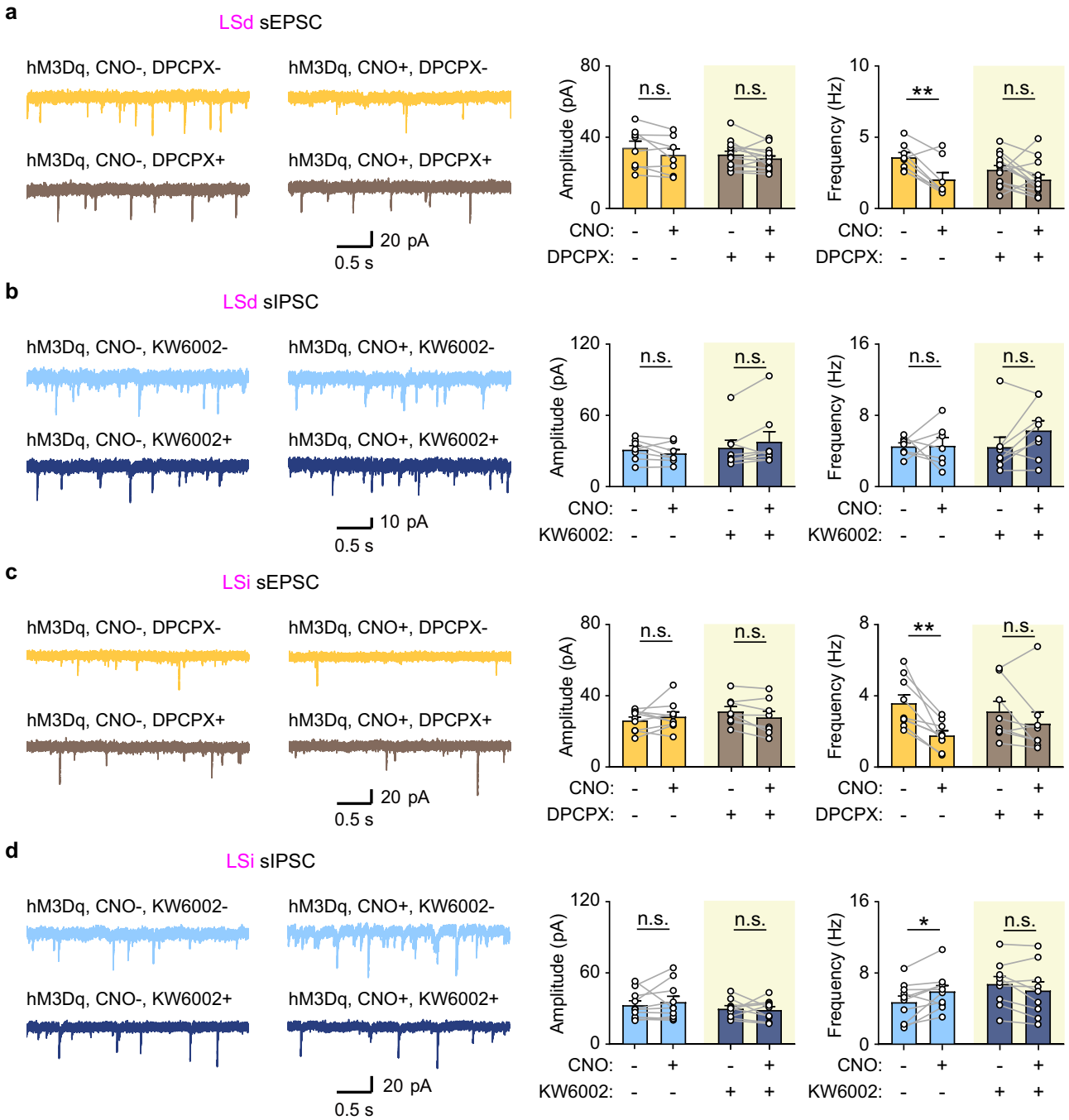

Fig. 4 | Astrocytic modulation of synaptic transmissions in the LS is mediated by adenosine receptors. Voltage-clamp recordings of LS neurons in acute septal slices expressing hM3Dq in LS astrocytes. Representative traces, along with quantification of the amplitude and frequency of sEPSCs and sIPSCs, were recorded from LSd neurons (**a**, **b**) and LSi neurons (**c**, **d**) adjacent to hM3Dq-expressing astrocytes. Note that DPCPX, the A_1R antagonist, reduces the astrocytic manipulation-induced reduction in sEPSC frequency in LSd and LSi neurons (**a**, **c**), while KW6002, the $A_{2A}R$ antagonist, prevents the astrocytic manipulation-induced increase in sIPSC frequency in LSi neurons only (**b**, **d**). The number of samples and the associated statistical details are listed in Supplementary Data 1. Source data are available in the Source Data file. $^*p < 0.05$, $^{**}p < 0.01$, n.s., not significant. The data are presented as the mean ± SEM.

neurons through a subregion-specific differential modulation of presynaptic inputs by activating different adenosine receptor subtypes.

Astrocytes induce excitation of LS neurons in regions with low or absent hM3Dq expression

We examined c-Fos expression in the LS following chemogenetic stimulation of LSd or LSi astrocytes with hM3Dq (Fig. 5a, e). LS sections from mice with hM3Dq-manipulated LSd astrocytes contained a significantly higher number of c-Fos immunoreactive astrocytes and neurons in the LSd compared to control mice expressing mCherry (Fig. 5b). A detailed analysis revealed that c-Fos expression in LSd astrocytes was primarily localized to regions where hM3Dq was highly expressed. In contrast, c-Fos expression in LSd neurons was predominantly found in regions with low or absent hM3Dq expression (Fig. 5c). c-Fos induction resulting from LSd astrocytic manipulation was also observed in the LSi, where astrocytic hM3Dq expression is absent. Most c-Fos immunoreactive neurons were located in the anterior LSi (Bregma 0.8–0.4 mm) (Fig. 5d). Similarly, manipulation of

https://doi.org/10.1038/s41467-024-54376-x

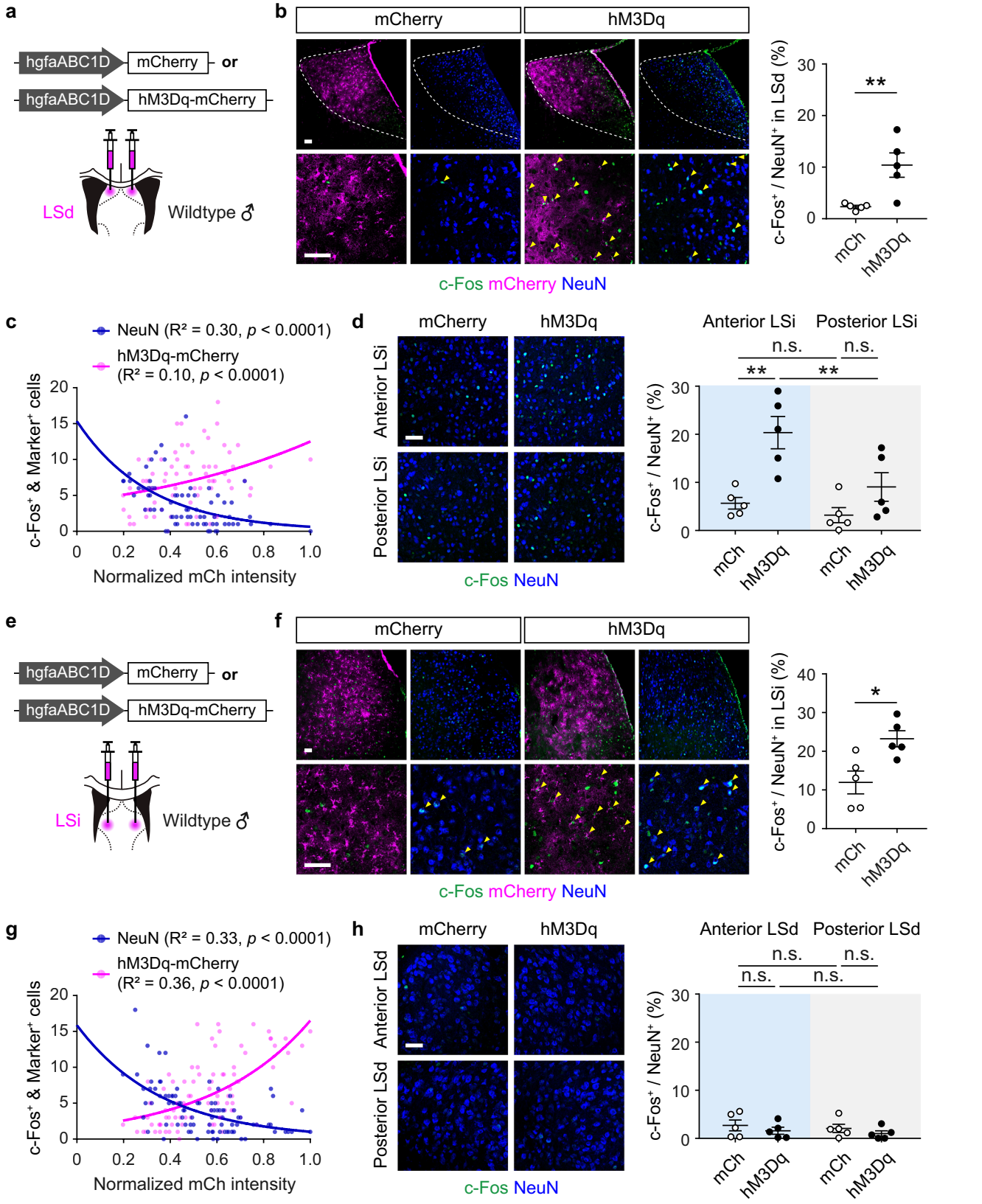

LSi astrocytes induced c-Fos expression in LSi neurons (Fig. 5e–g). In contrast to LSd astrocytes, manipulating LSi astrocytes failed to induce c-Fos expression in LSd neurons, indicating a lack of communication between LSi astrocytes and LSd neurons (Fig. 5h). Together with our electrophysiological findings, these results suggest that astrocytes in the LSd and LSi suppress the excitation of neighboring neurons in the LS while facilitating the activation of distant neurons within the same or adjacent LS subregions. Given the unidirectional communication from LSd to LSi, but not vice versa, neural circuits involving inhibitory neurons, rather than the diffusion of signaling molecules through astrocyte networks connected via gap junctions, may regulate sub-regional communication in LS.

Fig. 5 | LS astrocytes induce neuronal c-Fos in LS regions where hM3Dq expression is low or absent. The AAV hgfaABC1D-mCherry (*mCh*) or hM3Dq-mCherry (*hM3Dq*) was injected into either the LSd (**a**) or LSi (**e**) of wild-type mice. c-Fos expression elicited by astrocytic manipulation in targeted regions (**b**, **f**). Native fluorescence of mCherry and hM3Dq-mCherry in LS astrocytes (*magenta*) and immunoreactivities of c-Fos (*green*) and NeuN (*blue*) in the LSd (**b**, left) and LSi (**f**, left). Arrows indicate c-Fos$^+$ cells that overlapped with mCherry or NeuN. Quantification of c-Fos$^+$ neurons in the whole LSd (**b**, right) and LSi (**f**, right). The correlation between hM3Dq-mCherry fluorescence intensity and the number of c-Fos$^+$ astrocytes (hM3Dq-mCherry, *magenta*) or neurons (NeuN, *blue*) was assessed via Poisson regression modeling (**c**, **g**). R^2 is the coefficient of determination. Neuronal c-Fos was induced in the neighboring region that was not targeted by the virus (**d**, **h**). Note that only chemogenetic manipulation of LSd astrocytes induced c-Fos expression in the LSi, not vice versa. *Anterior LSi* or *LSd* (bregma 0.8-0.4 mm), *posterior LSi* or *LSd* (bregma 0.4-0.0 mm). Scale bars, 50 μm. The number of samples and the associated statistical details are listed in Supplementary Data 1. Source data are available in the Source Data file. $^*p < 0.05$, $^{**}p < 0.01$, n.s., not significant. The data are presented as the mean ± SEM.

To investigate whether astrocyte-induced c-Fos expression occurs in LS neuronal populations responsive to aversive stimuli, we performed an RNAscope analysis using probes targeting *c-Fos*, *Crhr2*, *Nts*, and *Gad1* (used as a marker for LS neurons). Our results indicate that hM3Dq-mediated manipulation of LSd or LSi astrocytes significantly increased the number of *c-Fos*$^+$ and *Gad1*$^+$ cells co-expressing *Crhr2* or *Nts* across the entire LS, compared to CNO-treated astrocytes expressing mCherry (Supplementary Fig. 8a–d). LSd astrocyte-induced neuronal *c-Fos* overlapped more with *Nts* than with *Crhr2*, while LSi astrocyte-induced neuronal *c-Fos* tended to overlap more with *Crhr2* than with *Nts* (Supplementary Fig. 8b, d). LSd astrocyte-induced *c-Fos* was observed in 8.8% of *Crhr2*$^+$ neurons in the LS, representing 11.0% of *c-Fos*$^+$ neurons (Supplementary Fig. 8e). LSd astrocyte-induced *c-Fos*$^+$ was expressed in 32.4% of *Nts*$^+$ neurons in the LS, representing 60.9% of *c-Fos*$^+$ neurons (Supplementary Fig. 8e). LSi astrocyte-induced *c-Fos* was detected in 42.4% of *Crhr2*$^+$ neurons in the LS, which accounted for 36.5% of *c-Fos*$^+$ neurons (Supplementary Fig. 8f). Lastly, LSi astrocytes induced *c-Fos* expression in 31.4% of *Nts*$^+$ neurons, accounting for 23.9% of *c-Fos*$^+$ neurons (Supplementary Fig. 8f). These findings suggest that LSd astrocytes may preferentially affect a subset of *Nts*$^+$ neurons, whereas LSi astrocytes may have a slightly greater influence on a subset of *Crhr2*$^+$ neurons compared to *Nts*$^+$ neurons.

Subregional localization of LS astrocytes enables specific stress responses

To investigate the physiological and behavioral consequences of intracellular Ca^{2+} increases in astrocytes across LS subregions, we then injected an AAV expressing the hgfaABC1D promoter-driven hM3Dq or mCherry into the LSd or LSi (Fig. 6a, i). Upon administration of CNO, mice expressing hM3Dq in LSi astrocytes exhibited an increase in heart rate and blood corticosterone levels (Fig. 6b, c). Except for marble-burying behavior, hM3Dq-mediated manipulation did not elicit behavioral changes, such as anxiety-like behaviors, social interactions, or defensive responses to aversive sensory stimuli (Fig. 6d and Supplementary Fig. 9a–f). Also, this manipulation did not influence behaviors in mice subjected to subthreshold social defeat stress (SSDS) (Fig. 6e–h and Supplementary Fig. 10a–d).

In contrast, activation of LSd astrocytes using hM3Dq in unstressed mice did not noticeably change heart rate, blood corticosterone levels, marble-burying behavior, defensive behaviors elicited by threat-like stimuli, food intake, forced swimming, home cage social interactions, anxiety-like behavior, or social interaction with a novel aggressor (Fig. 6i–l and Supplementary Fig. 9g–o). Even repetitive treatments with CNO for 10 days before behavioral testing had no impact on anxiety-like behavior or social interaction (Supplementary Fig. 9p). However, when mice were subjected to SSDS, hM3Dq-mediated manipulations showed enhanced anxiety-like behavior in the open field and elevated plus maze tests, as well as social avoidance toward a novel aggressor (Fig. 6m–o). This manipulation also significantly increased the proportion of mice susceptible to social defeat stress (Fig. 6p). Finally, the combined application of SSDS and hM3Dq-mediated LSd astrocyte manipulation increased heart rate, while blood corticosterone levels remained unaffected (Supplementary Fig. 9q, r and Supplementary Fig. 10e, f). Histological analysis revealed that combined astrocytic hM3Dq manipulation and SSDS increased c-Fos induction in LSd neurons, particularly in areas with low or absent hM3Dq expression (Fig. 6q, r). In summary, our findings suggest that astrocytes in the LSi can generate a sympathetic response and stress hormone release in stress-naïve mice, whereas their effects on behavior, regardless of stress experience, are limited. On the other hand, astrocytes in the LSd do not appear to influence sympathetic or hormonal responses under unstressed conditions, but they can promote increases in heart rate, as well as anxiety and social avoidance in mice exposed to SSDS.

Social avoidance induced by acute and chronic social defeat stress requires LSd astrocytes

Subsequently, we investigated the impact of suppressing Ca^{2+} increases in LS astrocytes on behavioral responses to aversive and stressful stimuli by expressing the plasma membrane Ca^{2+} pump, hPMCA2w/b, in astrocytes (Fig. 7a and Supplementary Fig. 1f). Overexpressing hPMCA2w/b can suppress astrocyte calcium elevation[43,44]. In unstressed mice, hPMCA2w/b expression in astrocytes did not significantly change threat-induced avoidance or defensive behaviors, social interactions, or anxiety levels (Fig. 7b–d and Supplementary Fig. 11a–i, m-q). In contrast, manipulating LSd astrocytes with hPMCA2w/b in mice subjected to acute social defeat stress (ASDS) alleviated anxiety-like behavior in the open-field test and reduced social avoidance (Fig. 7e–h and Supplementary Fig. 10g–k). Moreover, this manipulation increased the proportion of mice who were resilient to social defeat stress (Fig. 7i). Overexpressing hPMCA2w/b in LSd astrocytes also mitigated chronic social defeat stress (CSDS)-induced social avoidance (Fig. 7j–n and Supplementary Fig. 10l–o). These results demonstrate the essential role of LSd astrocytes in mediating social avoidance during both acute and chronic social defeat stress, as well as their participation in stress-induced anxiety. In contrast, LSi astrocytes were not required for these behaviors, despite the presence of stress experiences (Supplementary Fig. 11j–l).

Discussion

Here, we show that astrocytes in the LS regulate specific stress responses in a spatially restricted manner. Furthermore, we have revealed that astrocytes influence the activity of LS neurons through subregion-specific inhibitory and activation mechanisms. Astrocytes in the LSd subregion do not affect autonomic or hormonal stress responses under unstressed conditions but enhance heart rate, anxiety-like behavior, and social avoidance in mice exposed to social defeat stress. At the local circuit level, astrocytes in the LSd inhibit neighboring neurons by suppressing presynaptic excitatory inputs through A_1R. Astrocytes in the LSi inhibit presynaptic excitatory inputs through A_1R activation while simultaneously increasing inhibitory synaptic transmission through $A_{2A}R$, which leads to the inhibition of nearby neurons in the LSi. Both LSd and LSi astrocytes simultaneously promote the activation of neurons distant from the manipulated astrocytes. To provide further mechanistic insight into the underlying processes of the stress response, we demonstrated that LS astrocytes displayed increased intracellular Ca^{2+} levels when exposed to aversive

https://doi.org/10.1038/s41467-024-54376-x

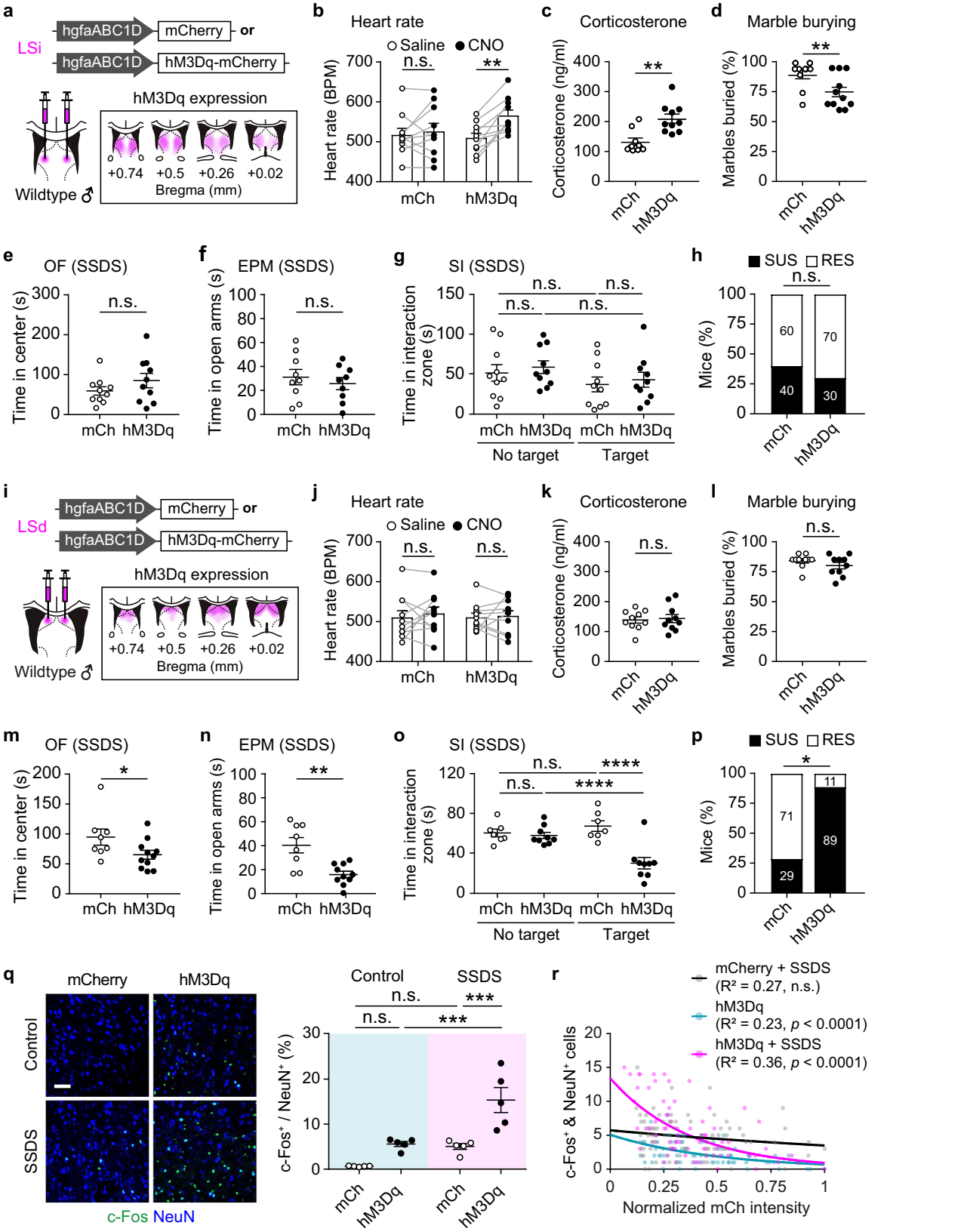

sensory stimuli and stressful environments. These astrocytic responses are induced by neural inputs originating from the hippocampus. Taken together, our data suggest that astrocytes shape neuronal responses in the LS to integrate environmental information and contribute to generating appropriate physiological and behavioral responses in a subregion-specific manner (Supplementary Fig. 12).

Aversive and stressful stimuli such as physical restraint, social defeat, and morphine withdrawal activate the LS, leading to a characteristic crescent-shaped pattern of c-Fos expression and 2-deoxyglucose uptake along the dorsoventral axis of the LS[5,45]. In addition, in vivo Ca^{2+} recordings of LS neurons reveal dynamic changes in intracellular Ca^{2+} levels in response to aversive, rewarding, or

https://doi.org/10.1038/s41467-024-54376-x

Fig. 6 | Astrocytes contribute to specific aspects of stress responses depending on their subregional localization in the LS. The AAV hgfaABC1D-mCherry (*mCh*) or hM3Dq-mCherry (*hM3Dq*) was injected into the LSi or LSd of wild-type mice (**a**, **i**). The representative viral expression of hM3Dq is indicated in the brain images (**a**, **i**, *magenta*). Heart rate (**b**, **j**), blood corticosterone level (**c**, **k**), and marble burying behavior (**d**, **l**) in unstressed mice. Anxiety-like behaviors (**e**, **f**, **m**, **n**) and social interaction (*SI*, **g**, **h**, **o**, **p**) were assessed in mice previously subjected to subthreshold social defeat stress (*SSDS*). The percentage of mice exhibiting an SI ratio < 1 (susceptible, *SUS*) or an SI ratio ≥ 1 (resilient, *RES*) among mice treated with SSDS (**h**, **p**). c-Fos was induced by hM3Dq-mediated manipulation of LSd astrocytes in the absence (*Control*) or presence (*SSDS*) of SSDS (**q**, left). Quantification of c-Fos (*green*) expression in neurons (NeuN, *blue*) (**q**, right). The correlation between mCherry fluorescence intensity (SSDS only, mCherry in LSd astrocytes, *black*; hM3Dq in LSd astrocytes, *cyan*; SSDS and hM3Dq, *magenta*) and the number of c-Fos$^+$ neurons, as determined by Poisson regression modeling (**r**). R^2 is the coefficient of determination. Scale bars, 50 μm. The number of samples and the associated statistical details are listed in Supplementary Data 1. Source data are available in the Source Data file. $^*p < 0.05$, $^{**}p < 0.01$, $^{***}p < 0.001$, $^{****}p < 0.0001$, n.s., not significant. The data are presented as the mean ± SEM.

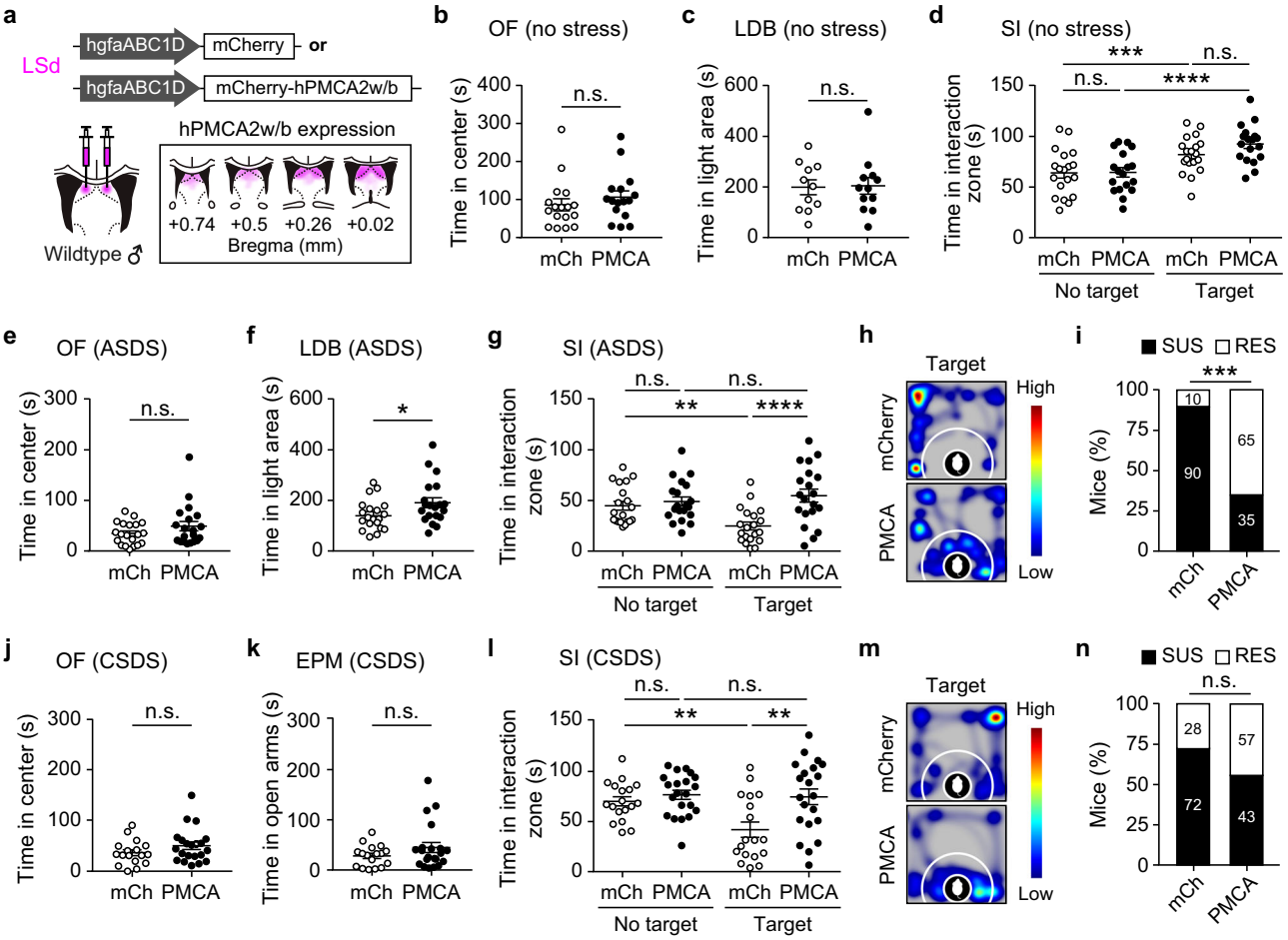

Fig. 7 | Astrocytes in the LSd are necessary for social avoidance caused by acute and chronic social defeat stress. hPMCA2w/b (*PMCA*) or control mCherry (*mCh*) was expressed in LSd astrocytes (**a**). The representative hPMCA2w/b-expressing area is depicted in magenta in the brain images. The behavioral effects of hPMCA2w/b expression in unstressed mice (**b**–**d**, *no stress*) and mice subjected to acute social defeat stress (**e**–**i**, *ASDS*) or chronic social defeat stress (**j**–**n**, *CSDS*) were assessed via the open field test (*OF*, **b**, **e**, **j**), light-dark box test (*LDB*, **c**, **f**), elevated plus maze test (*EPM*, **k**), and social interaction test (*SI*, **d**, **g**–**i**, **l**–**n**). A representative heatmap illustrating the time a subject mouse spent in compartments in the social interaction test (**h**, **m**). The percentage of mice susceptible (*SUS*) or resilient (*RES*) to social defeat stress (**i**, **n**). The number of samples and the associated statistical details are listed in Supplementary Data 1. Source data are available in the Source Data file. $^*p < 0.05$, $^{**}p < 0.01$, $^{***}p < 0.001$, $^{****}p < 0.0001$, n.s., not significant. The data are presented as the mean ± SEM.

stressful stimuli in awake animals. For example, NTS$^+$ and CRHR2$^+$ neurons, which are primarily localized in the intermediate and ventral LS, exhibit increased Ca^{2+} levels in response to nociceptive and threat-related stimuli[15,17]. SST$^+$ neurons located in the LSd display increased Ca^{2+} levels in response to electric shocks and anxiogenic environments but show a decrease in Ca^{2+} during freezing in fear-associated contexts[9,46]. Overall, despite differences in their functions and distribution patterns within the LS, these subsets of neurons exhibit increased intracellular Ca^{2+} levels in response to stimuli that provoke avoidance or withdrawal behaviors. We note the challenges of identifying specific responses in the anatomical compartments, as each neuronal population spans multiple subdomains within the LS and displays some degree of overlap with other populations. Furthermore, studies employ different types of stimuli, making it difficult to compare Ca^{2+} responses among these neuronal populations. Our systematic analysis of astrocytic responses to a consistent set of stimuli across various LS subregions indicates that LS astrocytes exhibit remarkably similar Ca^{2+} responses despite the observed functional heterogeneity in LS subregions. The functional consequences of the simultaneous activation of astrocytes in disparate LS subregions have

not been fully elucidated. In addition, whether there are subpopulations of astrocytes selectively responding to a subset of those aversive stimuli in a given subregion has yet to be determined.

The physiological and behavioral roles of LS astrocytes show some similarities but do not entirely replicate the reported functions of LS neurons. For example, LSi astrocytes increased heart rate and elevated corticosterone levels, similar to the effects induced by optogenetic activation of CRHR2$^+$ neurons, which are highly concentrated in the LSi[6,15]. CRHR2$^+$ neurons can also enhance defensive behavior and anxiety-like behaviors. However, astrocytes in the LSi did not phenocopy these functions. Our RNAscope analysis revealed that hM3Dq-mediated manipulation of LSi astrocytes induced *c-Fos* mRNA expression in a subset of *Crhr2*$^+$ neurons (42.4%), suggesting a potential connection between astrocyte- and *Crhr2*$^+$ neuron-mediated functions. The partial overlap may also explain the partial recapitulation of the observed phenotypes. In contrast, a prominent overlap was observed between *c-Fos* mRNA induced by hM3Dq-mediated manipulation of LSd astrocytes and *Nts*$^+$ neurons, a neuronal population involved in social avoidance. Whether the activation of astrocyte-driven subsets of *Crhr2*$^+$ or *Nts*$^+$ neurons can recapitulate the physiological and behavioral phenotypes elicited by LSi and LSd astrocytes, respectively, requires further study.

Unlike LSi astrocytes, LSd astrocytes underlie anxiety-like behaviors and social avoidance in mice exposed to social defeat stress. A primary neuronal population in the LSd, SST$^+$ neurons, can alleviate anxiety- and depressive-like behaviors and promote social interaction in stressed mice[27,28]. Given the inhibitory effect of LSd astrocytes on local neurons, we posit that LSd astrocytes directly inhibit SST$^+$ neurons, potentially disinhibiting anxiogenic and social avoidance-promoting neurons within or outside the LS that were previously under inhibitory control by SST$^+$ neurons[46,47]. In line with this, we found that LSd astrocytes drive neuronal excitation in the LSi region where NTS$^+$ neurons are highly populated[16]. Thus, future studies will examine LS astrocyte-neuron circuit dynamics to elicit specific functional phenotypes.

Growing evidence has demonstrated the functional implications of lateral inhibition between LS neurons[25]. For example, inhibitory controls among LS neurons play a crucial role in activating the ventrolateral part of the ventromedial hypothalamus (VMHvl) neurons and promoting inter-male aggression[24]. Stimulation of glutamatergic afferents into the LS initially induces an excitatory synaptic potential, followed by a hyperpolarizing potential in LS neurons[48,49]. In addition, the activation of specific neuronal subsets, such as adenosine A_{2A} receptor$^+$, oxytocin receptor$^+$, or vasopressin receptor 1A$^+$ neurons, leads to an overall reduction in neural activity or an increase in tonic inhibitory transmission within the LS[50,51]. We demonstrated that c-Fos expression induced by hM3Dq, an astrocytic manipulation, negatively correlates with the expression level of the effector molecule. Slice electrophysiology further revealed that LS astrocytes inhibit neighboring neurons while reducing inhibitory inputs to distant neurons. Combined with prior studies on lateral inhibition between GABAergic neurons within the LS, we hypothesize that astrocyte-promoted inhibition of nearby GABAergic neurons may disinhibit other LS neurons in local neural circuits by relieving lateral inhibition. Further research will establish the synaptic connectivity among oppositely regulated LS neurons and clarify the causal relationship between astrocyte-driven inhibition and activation in these local circuits.

Astrocytes play a critical role in regulating neural circuit activity through various mechanisms[52]. They can influence the intrinsic properties of neighboring neurons[53,54]. In addition, astrocytes modulate synaptic transmission to local neurons and impact the structure of dendritic spines and synapses[29,55]. Our study revealed that astrocytes in the LS modulate neighboring neurons by affecting their synaptic inputs without altering their intrinsic electrophysiological properties. We also found that astrocytes in different subregions of the LS employ distinct modulatory mechanisms on neural inputs. LSd astrocytes inhibit excitatory synaptic inputs to LSd neurons by activating G_i-linked A_1Rs. LSi astrocytes utilize an additional mechanism, strengthening inhibitory synaptic inputs to LSi neurons by activating G_s-linked A_{2A}Rs. We suspect that these regulatory effects on excitatory and inhibitory synaptic inputs impact the excitatory-inhibitory balance of LS neurons.

Extracellular adenosine signaling can impact neuronal activity by reducing sEPSC frequency through A_1Rs and increasing sIPSC frequency through A_{2A}Rs in several brain regions, including the LS[50,56–59]. For example, adenosine inhibits glutamatergic input from the hippocampus to the LS in rats[59]. A recent study has revealed that A_{2A}R-mediated signaling is crucial for the inhibitory regulation of LS neurons. The A_{2A}R agonist CGS21680 increased spontaneous firing in $A_{2A}R^+$ LS neurons and elevated the sIPSC frequency in neighboring $A_{2A}R^-$ neurons[50]. However, the source of extracellular adenosine was not determined. Consistent with these findings, we observed an increase in the frequency of sIPSCs in LSi neurons upon treatment with CGS21680. We contend that it is unlikely that $A_{2A}R^+$ neurons, comprising approximately 1% of LS neurons, were included in our random selection of recorded neurons[50,60].

It is intriguing to hypothesize that astrocytes in the LSi may serve as a major source of extracellular adenosine, which binds to and promotes the spontaneous firing of $A_{2A}R^+$ neurons in the LSi, subsequently suppressing $A_{2A}R^-$ neurons. Evidence for this hypothesis comes from eliminating the A_{2A}R-mediated inhibitory effects of LSi astrocytes when inhibiting the spontaneous firing of LS neurons, as shown by our mIPSC recordings. Further research will elucidate how astrocytes modulate local LS circuitry and functions, including recordings from molecularly defined neural populations such as $A_{2A}R^+$ and $A_{2A}R^-$ neurons[50]. Employing mouse genetic tools such as Cre driver mouse lines will be essential for visualizing and recording rare, elusive LS neuronal populations. Pharmacological manipulation of adenosine receptors in septal slices highlighted the role of extracellular adenosine in astrocyte-neuron communication. However, direct measurements of adenosine release from astrocytes are lacking. Thus, determining in vivo whether astrocytes release adenosine or whether adenosine is generated from released ATP is important for characterizing adenosine signaling mechanisms in the LS. Lastly, our findings presented here underscore assessing these molecular mechanisms in septal slices from socially stressed mice.

The regulatory effect of astrocytes on local neural circuits in the LS not only supports a conserved role for astrocyte-neuron interactions in driving functional phenotypes but also reveals similarities in neuron-astrocyte interaction mechanisms in another brain region composed exclusively of inhibitory neurons, the CeA[61]. Astrocytes in the CeA inhibit excitatory synapses from the basolateral amygdala by activating the A_1 adenosine receptor while activating inhibitory synapses from the lateral subdivision of the CeA through the A_{2A} receptor, leading to a reduction in fear expression[57]. A growing body of evidence suggests reciprocal inhibitory controls between molecularly and functionally defined neuronal subpopulations in this region[62,63]. Shifting the balance of populational activities may facilitate rapid behavioral switching[62,64]. These two distinct brain regions, which play roles in mediating emotional responses, likely share molecular and neural circuit mechanisms involving astrocytes to fine-tune regional neural activities, potentially promoting scaled functional outcomes.

In summary, this study advances the role of astrocytes in the LS, their responses to aversive stimuli, and their modulation of LS neuronal activity and stress responses. Understanding astrocytic contributions to the molecular, synaptic, and neural circuit levels enhances comprehension of how the LS integrates information to produce affective behaviors, providing insights into general principles governing brain regions with predominant GABAergic neuronal subpopulations. Overall, our findings may suggest conserved principles

that specify the interactions between astrocytes and neurons to drive behavioral states.

Methods

Animals

All animal experiments were approved by the Institutional Animal Care and Use Committee of the Daegu Gyeongbuk Institute of Science & Technology (DGIST-IACUC-20011502-08, DGIST-IACUC-24080101-0000) and followed the guidelines of the National Institutes of Health (NIH). Vglut2-Cre mice (The Jackson Laboratory, stock no. 016963), were used in these experiments. Wildtype C57BL/6 J mice (C57BL/6JBomTac) and retired CD-1 breeder males were obtained from DBL (South Korea). Mice were housed and maintained under a 12-hour light/dark cycle, with lights on at 7 AM. The animals had free access to water and food throughout the study. For behavioral testing and social defeat stress experiments, 8- to-14-week-old C57BL/6 J mice were individually housed for at least 7 days prior to the respective procedures. CD-1 retired male breeders aged >3 months were used as aggressors in the social defeat stress models.

Virus

The following viruses were obtained from the Viral Vector Facility at the University of Zürich: AAV5-hgfaABC1D-hM3Dq-mCherry (6.0×10^{12} gc/ml, v97-5), AAV5-hgfaABC1D-mCherry (6.1×10^{12} gc/ml, v222-5), AAV5-hgfaABC1D-EGFP (7.0×10^{12} gc/ml, v95-5), and AAVretro-hEF1α-mCherry (7.6×10^{12} gc/ml, v212-retro). In addition, Addgene provided the following viruses: AAV5-hgfaABC1D-hM3Dq-mCherry (1.8×10^{13} gc/ml 50478-AAV5), AAV5-hgfaABC1D-cyto-GCaMP6f (1.3×10^{13} gc/ml, 52925-AAV5), AAV5-hgfaABC1D-mCherry-hPMCA2w/b (2.5×10^{13} gc/ml, 111568-AAV5), AAV1-hSyn-GCaMP6s (2.5×10^{13} gc/ml, 100833-AAV5), AAV2-hSyn-DIO-hM4Di-mCherry (2.3×10^{13} gc/ml, 44362-AAV2), AAV2-hSyn-DIO-mCherry (2.1×10^{13} gc/ml, 50459-AAV2), and AAV5-hSyn-FLEX-rc[ChrimsonR-tdTomato] (2×10^{13} gc/ml, 62723-AAV5). AAV9-hgfaABC1D-GCaMP8s (1.5×10^{13} gc/ml) was generated by using a pGP-AAV-syn-jGCaMP8s-WPRE (Addgene, 162374).

Stereotaxic surgery

The AAV vector was administered to the target brain region through stereotaxic surgery, following the protocol described previously[65]. A mouse was initially anesthetized by placing it in an induction chamber containing 2.5% isoflurane mixed with oxygen. The mouse received the anesthetizing gas (1–2%), continuously delivered through a nosecone (David Kopf Instruments), while being quickly positioned in a stereotaxic frame. Before surgery, the eyes were lubricated with Liposic ophthalmic gel (Bausch Health Korea, Carbomer). An incision was made in the scalp, and a hole was drilled in the skull above the intended target brain region.

The viral solution in a pulled glass micropipette (World Precision Instruments, 504949) was injected into the lateral septum (LS) at 20–40 nl/min with a nanoliter injector (World Precision Instruments, 300704) and SMARTouch controller (World Precision Instruments, MICRO2T). The injection coordinates were determined based on the mouse brain in stereotaxic coordinates[34]: LSd, ± 0.37 mm ML, + 0.10 mm AP, − 2.60 mm DV; LSi, ± 0.50 mm ML, + 0.60 mm AP, − 3.50 mm DV; hippocampus, ± 1.10 mm ML, − 2.40 mm AP, − 1.50 mm DV; ± 2.65 mm ML, − 2.40 mm AP, − 2.40 mm DV; ± 2.30 mm ML, − 3.00 mm AP, − 1.80 mm DV; infralimbic cortex, ± 0.30 mm ML, + 1.50 mm AP, − 2.85 mm DV; and lateral hypothalamus, ± 1.10 mm ML, − 1.0 mm AP, − 5.10 mm DV. The injection sites for fiber photometry are indicated in Supplementary Fig. 1g. The injection volumes per hemisphere were 80–200 nl (AAV5-hgfaABC1D-EGFP, AAV5-hgfaABC1D-mCherry, AAV5-hgfaABC1D-hM3Dq-mCherry, and AAV5-hgfaABC1D-mCherry-hPMCA2w/b, bilateral), 300–500 nl (AAV5-hgfaABC1D-cyto-GCaMP6f, AAV9-hgfaABC1D-GCaMP8s, AAV1-hSyn-GCaMP6s, AAV2-hSyn-DIO-hM4Di-mCherry, AAV5-hSyn-FLEX-rc[ChrimsonR-tdTomato], and AAV2-hSyn-DIO-mCherry), and 40 nl (AAVretro-hEF1α-mCherry, unilateral). For the unilateral injection, targeting of the left and right hemispheres was counterbalanced.

After the virus injection, the capillary was slowly retracted, and the scalp incision was closed using a tissue-adhesive bond (3 M, Vetbond, 084-1469SB). If necessary, a ferrule cannula (200 μm in core diameter, 3.2–4.0 mm long, 0.48 N.A., Newdoon, China) was implanted approximately 100–200 μm above the virus injection site and secured to the skull with dental cement (Sun Medical, Japan). The mouse was then injected with ketoprofen (i.p., 2 μg/g body weight, Unibiotech, South Korea) before being returned to its home cage. Ibuprofen (0.2 mg/ml, Hanmi Pharmaceutical, South Korea) was provided in the drinking water for at least 3 days after surgery. The mice were individually housed and allowed to recover for at least 4 weeks before behavioral assays and slice recordings were conducted.

Fiber photometry

A 465 nm LED light (Doric Lenses, LEDD_2), passed through a fluorescence mini-cube (Doric Lenses, FMC6_IE(400-410)_E1(460-490)_F1(500-540)_E2(555-570)_F2(580-680)_S), was delivered to the target brain region via a patch cord (400 μm core diameter, 0.48–0.54 N.A., Doric Lenses) and a ferrule cannula (200 μm core diameter, 0.48 N.A., Newdoon). The excitation light was modulated at 320 or 330 Hz using the RZ5P fiber photometry processor (Tucker-Davis Technologies) running Synapse software (Tucker-Davis Technologies). The light intensity was maintained below 50 μW at the tip of the ferrule cannula. The emitted light was passed through a mini-cube, collected by a Femtowatt photoreceiver (Newport Corporation, 2151), and processed at 1 kHz using the RZ5P processor. The acquired signals were then adjusted to a sampling rate of 120 Hz using MATLAB R2022b (MathWorks). $\Delta F/F$ was calculated as $(F_{465} - F_0) / F_0$, where F_0 represents the median of the baseline fluorescence.

Fiber photometric recordings were conducted in a controlled environment without background noise or prominent visual cues. Before the experiments, all mice were acclimated to the testing equipment for 20 min, and baseline GCaMP6f signals were recorded for 5–10 min. The GCaMP6f-expressing mice were then exposed to various sensory, social, or stressful stimuli. Simultaneously, mouse behavior was recorded using a video camera (Logitech, 960-000770). Recordings were conducted in the home cage, except for the looming disk and electric shock stimuli, which required specialized equipment. Food and fluid intake tests were performed in a plexiglass cylinder. For the "approaching hand" stimulus, the experimenter's hand was swiftly lowered from 40 cm to 3–5 cm above the cage floor without making physical contact with the mouse. The interval between stimuli varied from 3 to 15 seconds. The looming disk or drifting grating stimuli were presented to the mouse after a 5-minute baseline recording, with the mouse positioned in the middle part of the testing arena. The size of the looming disk increased linearly from 0° to 40° in 0.5 sec and remained at 40° for 33 ms. This procedure was repeated 15 times within 8 sec. Upon exposure to a looming disk stimulus, a mouse can exhibit both fleeing and freezing behaviors, with fleeing being more prevalent under our testing conditions. The fleeing response typically occurred immediately after the onset of the looming disk, whereas freezing behavior manifested with a more prolonged delay following the stimulus. Astrocytic Ca^{2+} elevation occurred within seconds after the stimulus presentation and aligned more closely with the timing of fleeing behavior. However, there were instances when fleeing or freezing behaviors did not accompany astrocytic Ca^{2+} transients. Therefore, astrocytic Ca^{2+} changes seem to correlate more strongly with the stimulus itself than with specific defensive behaviors.

The drifting grating stimulus consisted of alternating black and gray lines (each 4.5 cm in width), moving at a speed of 14 cm/s on an overhead computer monitor for 8 sec. Electric foot shocks (0.3 mA, 0.5 sec) were administered to the mouse using a fear conditioning

system (Lafayette Instrument, 80014CGAT). In the case of the startling acoustic stimulus, white noise with intensity increasing from 0 to 80 dB in 1 sec was played 10 consecutive times using a mobile speaker (Axxen, BS11). A predator odor, trimethylthiazoline (TMT, 20 µl, 90%, BioSRQ), was applied by dropping the solution onto a piece of filter paper placed in a corner of the mouse's cage (35 cm × 14 cm × 13 cm). Some mice exhibited a brief Ca^{2+} response to the approaching hand during the pipetting procedure. In the denatonium benzoate (bitter compound, 1 mM, Sigma-Aldrich, D5765), sucrose (2%, Duchefa Biochemie, S0809), or food intake experiments, mice that had been deprived of water (for denatonium benzoate or sucrose intake) or food for more than 12 h were given a water bottle containing denatonium benzoate or sucrose or received food pellets, respectively. The rotarod test involved placing the mouse on a rotating wheel (Ugo Basile, 47650), initially set to 5 rpm for 3 min, which then accelerated to 40 rpm over 300 sec. The test concluded when the mouse fell off the wheel. The resident-intruder test was conducted in the mouse's cage, with a CD-1 aggressor, C57BL/6 male, or C57BL/6 female mouse introduced, and the test then proceeded for 5–15 min. An attack was scored from the onset of biting. Restraint and tail suspension stresses were applied by gently wrapping and holding the mouse's entire body in the experimenter's hand for 1-2 min and by securing the mouse's tail to the wall with tape for 1-2 min, respectively. For stimuli that required locating the subject mouse to test equipment, astrocytic Ca^{2+} levels increased during handling ('hand approach') but quickly returned to pre-handling levels afterward.

To identify the neural mechanisms driving astrocytic Ca^{2+} increase, mice expressing GCaMP6f or GCaMP8s in LS astrocytes and hM4Di in an upstream brain region (the hippocampus, infralimbic cortex, or lateral hypothalamic area) or the LS were injected i.p. with CNO (3 mg/kg) or saline (0.9% NaCl) 20 min before the fiber photometric recording. After a 10-minute baseline recording, they were stimulated with an approaching hand, a CD-1 aggressor, or an electric shock. To determine the sufficiency of the hippocampus for the astrocytic Ca^{2+} response, GCaMP6f-expressing LS astrocytes were recorded while hippocampal neurons expressing ChrimsonR or mCherry were optogenetically stimulated with a 635 nm light pulse (10 s duration, 20 Hz, 20 ms pulses). The frequency and duration of photostimulation were controlled using an Isolated Pulse Stimulator (A-M Systems). The light intensity was set to 10 mW for cell body activation and 15–20 mW for terminal activation.

To evaluate the intracellular Ca^{2+} levels of LS astrocytes and neurons before and after a stimulus or a chemogenetic or optogenetic manipulation, the mean $\Delta F/F$ was calculated during specific time windows, using the indicated event as the reference point: − 5 to 0 sec and 0 to 10 sec for astrocytic Ca^{2+} before and after all sensory and social stimuli, except for the following stimuli: − 5 to 0 sec and 0 to 60 sec for astrocytic Ca^{2+} before and after TMT; − 30 to − 20 sec and 0 to 60 sec for astrocytic Ca^{2+} before and after onset of restraint; − 20 to − 10 sec and 0 to 60 sec for astrocytic Ca^{2+} before and after initiation of tail suspension; − 5 to 0 sec and 0 to 5 sec for astrocytic Ca^{2+} before and after conclusion of restraint and tail suspension; − 20 to 0 sec and 80–100 sec for astrocytic Ca^{2+} when the rotarod speed was 5 rpm and 15 to 17 rpm; − 30 to − 20 sec and 0 to 20 min for neuronal Ca^{2+} before and after astrocytic manipulation using hM3Dq; and − 5 to 0 sec and 0 to 30 sec for neuronal Ca^{2+} before and after aversive stimuli while manipulating astrocytes using hPMCA2w/b. We chose to present the mean $\Delta F/F$, calculated by dividing the fluorescence during stimulation by the median fluorescence during baseline recordings because z-scores relying on the mean of baseline recordings, and the peak $\Delta F/F$ can be affected by intermittent noise-like signals observed during recording. Since the durations of baseline and stimulus application are unequal, AUC analysis is not suitable for our data.

Ex vivo electrophysiology

The LS of each wild-type male mouse was injected with AAV5-hgfaABC1D-mCherry or AAV5-hgfaABC1D-hM3Dq-mCherry. After a 4-week incubation period for viral expression, acute septal slices were prepared for ex vivo electrophysiological recordings. The mice were anesthetized using isoflurane and decapitated, and their brains were rapidly removed and placed in ice-cold, oxygenated dissection buffer (95% O_2 and 5% CO_2) with low Ca^{2+} and high Mg^{2+} concentrations. The dissection buffer consisted of 5 mM KCl, 1.23 mM NaH_2PO_4, 26 mM $NaHCO_3$, 10 mM dextrose, 0.5 mM $CaCl_2$, 10 mM $MgCl_2$, and 212.7 mM sucrose. Coronal lateral septal slices (300 µm) were cut and transferred to a holding chamber in an incubator filled with oxygenated artificial cerebrospinal fluid (ACSF). The ACSF contained 124 mM NaCl, 5 mM KCl, 1.23 mM NaH_2PO_4, 2.5 mM $CaCl_2$, 1.5 mM $MgCl_2$, 26 mM $NaHCO_3$, and 10 mM dextrose. The slices were maintained at 28–30 °C for a minimum of 0.5–1 h before recording. They were then moved to a recording chamber and continuously perfused (2 ml/min) with oxygenated ACSF (95% O_2 and 5% CO_2) at 25–27 °C. The virus-infected regions were identified by the native fluorescence of mCherry.

In whole-cell recordings, patch pipettes with resistances ranging from 4–8 MΩ were loaded with various internal solutions depending on the purpose of the recordings: for eEPSC-PPR and eIPSC-PPR recordings, the solution comprised 130 mM Cs-$MeSO_4$, 0.5 mM EGTA, 5 mM TEA-Cl, 8 mM NaCl, 10 mM HEPES, 1 mM QX-314, 4 mM ATP-Mg, 0.4 mM GTP-Na, and 10 mM phosphocreatine-Na_2. To measure the intrinsic properties of action potential firing and sEPSCs, the solution contained 135 mM K-gluconate, 8 mM NaCl, 10 mM HEPES, 2 mM ATP-Na, and 0.2 mM GTP-Na. For sIPSC recordings, the solution contained 105 mM K-gluconate, 30 mM KCl, 10 mM phosphocreatine-Na_2, 4 mM ATP-Mg, 0.3 mM GTP-Na, and 10 mM HEPES. All solutions were adjusted to a pH of 7.4, and the osmolarity was maintained at 280–290 mOsm.

The external recording solution was composed of ACSF, to which 100 µM picrotoxin was added for measuring sEPSCs and excitability, and 20 µM CNQX and 50 µM DL-AP5 were added for measuring sIPSCs. To measure mEPSCs and mIPSCs, TTX (1 µM, Alomone Labs, T-550) was added to the corresponding external solutions. Neurons were voltage-clamped at − 60 mV for recording eEPSCs and at 0 mV for recording eIPSCs. When necessary, CNO (10 µM) was introduced into the external solution. To evoke synaptic responses, 0.2 ms current pulses were applied using a concentric bipolar electrode positioned close to the recording regions to induce local synaptic transmission. The maximal amplitudes of EPSCs or IPSCs were determined, and 40–50% of each amplitude was employed to record the eEPSC-PPR and eIPSC-PPR. The A_1R antagonist DPCPX (1 µM, Tocris, 0439) or the $A_{2A}R$ antagonist KW6002 (300 nM, Sigma, SML0422) was administered to the external solution at least 15 min prior to recording spontaneous synaptic transmission. CCPA (the A_1R agonist, 1 µM, Sigma, C7938) and CGS21680 (the $A_{2A}R$ agonist, 30 nM, Tocris, 1063) were applied for at least 5 min to determine the effects of A_1Rs and $A_{2A}Rs$.

Recordings were conducted using a MultiClamp 700 A amplifier (Molecular Devices) with differential interference contrast illumination on an upright microscope (BX51WI; Olympus). Data acquisition and analysis were performed using pClamp 10.7 software (Molecular Devices). Only cells with an access resistance < 20 MΩ were recorded; those with an access resistance change >20% were excluded from the analysis. The signals were filtered at 3 kHz and digitized at 10 kHz using a DigiData 1550 system (Molecular Devices). Figure 3 and Supplementary Figs. 5, 7e–g compare responses from different cells treated with the indicated drugs, whereas Fig. 4, Supplementary Figs. 6, 7a–d present data from experiments comparing the same cells before and after drug treatment.

Heart rate

Heart rate was assessed using a blood pressure analysis system (Visitech Systems, BP-2000, Norway). A mouse expressing hM3Dq or control mCherry was administered CNO (3 mg/kg) and placed in a temperature-controlled box at 38 °C, with its tail exposed. A pressurizing device was utilized to apply pressure to the mouse tail, and photoplethysmography was employed to measure blood flow and heart rate from the mouse's tail.

Corticosterone level

A mouse expressing mCherry or hM3Dq-mCherry in LS astrocytes was subjected to a 30-minute treatment with CNO between 1:00 and 3:00 PM. After the mice were anesthetized with 5% isoflurane, blood was collected from the inferior vena cava and kept at room temperature for 30 min. Subsequently, the serum was separated from the blood by centrifugation at 21,206 × *g* for 30 min at 4 °C and stored at − 70 °C until the corticosterone level was determined.

A corticosterone ELISA kit (Enzo Life Science, Switzerland, ADI-900-097) was used to measure corticosterone levels. A standard curve was generated using serially diluted stock solutions of corticosterone. The serum sample was mixed with 0.01% Steroid Displacement Reagent (1:1), and the absorbance at 405 nm was measured using a Spark Multimode Microplate Reader (Tecan, Switzerland). The corticosterone concentration was calculated using the standard curve and Magellan software (Tecan, Switzerland).

Behavioral tests

Behavioral tests were conducted during the daytime. Prior to the tests, mice were habituated to the testing room for at least 30 min. Mouse behavior was scored by investigators who were blinded to the treatments.

Administration of clozapine N-oxide (CNO). For mice expressing hM3Dq-mCherry or a control fluorescent protein (EGFP or mCherry), CNO (3 mg/kg, Enzo Life Sciences, BML-NS105) dissolved in 0.9% NaCl was intraperitoneally administered. CNO was given 30 min before all behavioral assays and 20 min before the mice were subjected to sub-threshold social defeat stress (SSDS). In the case of chronic stimulation of LS astrocytes using hM3Dq, mice were injected i.p. with CNO (3 mg/kg) for 10 consecutive days from 9 to 10 AM. Control animals showed no detectable behavioral changes upon CNO administration.

Looming disk-evoked defensive behavior. The mouse was habituated to the test room for at least 3 h and then placed in a test box (35 cm × 35 cm × 35 cm) for 10 min. The illumination intensities in the test box and test room were 6 and 5 lux, respectively. On the test day, the mouse was moved to the test room and habituated for at least 3 hours in a home cage. After a 5-minute baseline recording in the test box, the mouse underwent visual stimulation with a rapidly expanding black disk displayed on an overhead monitor. The stimulus was initiated when the mouse moved to the middle part of the arena. The black disk on a gray background expanded exponentially from 5 to 40° in 0.75 sec and remained at 40° for 0.25 sec. This expansion-maintenance cycle was repeated 30 times consecutively within 30 sec. The stimulus was delivered to the animal three times in a test session, with at least a 30-second interval between stimuli. Mouse behavior was recorded using a video camera, and locomotive speed and immobility (>2 sec) were analyzed using EthoVision XT 11.5 (Noldus).

Acoustic startle behavior. The mouse was placed in an animal holder (2.85 cm diameter × 12.7 cm) inside a sound-attenuated acoustic chamber of the SR-LAB-startle response system (San Diego Instruments). The mouse was habituated to the 65 dB background white noise for 15 min. On the following day, after a 5-minute acclimation period, white noise of intensities 85, 90, and 95 dB was randomly delivered to the confined mouse for 20 ms. The interval between stimuli was 25 to 35 sec. The startle reflex of the animal was detected by the pressure sensor underneath the holder.

Electric shock-evoked freezing. The mouse was placed in a test chamber (20 cm × 20 cm × 20 cm) with a stainless-steel grid floor (Lafayette Instruments, 80014AT) The mouse was subjected to an electric foot shock (0.3 mA, 1 sec) five times using the Actimetrics Fear Conditioning Chamber Package (Lafayette Instruments, 80014AT), with 1-min intervals between stimuli for testing the effect of hM3Dq-mediated manipulation or 3-min intervals for hPMCA2w/b-mediated manipulation. Mobility was analyzed with the FreezeFrame 4 (Lafayette Instrument, AM1-FF04), and immobility of the mice for at least 1 sec was counted as freezing.

Shuttle-box test. The shuttle-box test was conducted using a Gemini active and passive avoidance system (San Diego Instruments, Gemini), consisting of two chambers with a stainless-steel grid floor (24.1 cm × 33 cm × 20.3 cm) and a gate between the chambers. The mouse was allowed to explore a randomly assigned chamber for 5 min and then stimulated with an electric foot shock (0.01–0.02 mA) for 10 sec, which caused it to escape to the other chamber. The test was performed ten times in a session with 30-second intervals between tests. The time from the onset of the electric foot shock to the time the mouse crossed the entire body to the other chamber was measured. The cut-off time was set at 10 sec.

Marble burying test. Dried glass marbles (1.2 cm diameter), washed in 70% ethanol and distilled water, were arranged in a 4 by 5 pattern on fresh bedding in a new cage (35 cm × 14 cm × 13 cm). A mouse was introduced into the cage with a filter-top cover and allowed to explore for 20 min. The number of marbles buried was manually counted.

Resident-intruder test. Male mice that were smaller and younger than resident males were used as intruders. Interactions between a resident and an intruder were recorded for 10 min using a video camera, and the time spent on the social investigation, attack, or chasing was manually scored.

Open field test. The test room was illuminated at 50 to 60 lux. The mouse was placed in the middle of a test box (38.8 cm × 38.8 cm × 34 cm), and its behavior was recorded for 10 min. Time spent in the center zone, a square area (23.28 cm × 23.28 cm) in the middle of the test box, was then analyzed using EthoVision XT 11.5 (Noldus).

Elevated plus maze test. The elevated plus maze consisted of two open arms (6.0 cm × 30.5 cm, 100 lux) and two closed arms (6.0 cm × 30.5 cm, 50 lux) with 25 cm walls surrounding the arms. The apparatus was positioned 50 cm above the floor. After the mouse was placed in the central zone, its behavior was recorded for 5 min using a video camera, and the time spent in the open arms was analyzed using EthoVision XT 11.5 (Noldus).

Light-dark box test. This test was performed in a test box (39.2 cm × 39.2 cm × 30.5 cm) consisting of light and dark compartments. The light side of the box was illuminated at 200 to 300 lux, and the dark side was illuminated at < 5 lux. A mouse was introduced into the dark side, and its behavior was recorded for 10 min. Time spent on the light side of the box was then analyzed using EthoVision XT 11.5 (Noldus).

Social interaction test. Social interaction was examined as previously described[66,67]. The illumination in the test room was kept at <5 lux. In the first session ("no target"), a C57BL/6 male mouse was introduced into a test box (38.8 cm × 38.8 cm × 34 cm) with an empty upside-down

pencil cup (10.5 cm × 23 cm). The subsequent session ("target") was conducted in the same test box with the pencil cup containing a CD-1 male mouse that the subject had never encountered before. The subject/s behavior was recorded for 150 s in each session via a video camera, and the time spent in the interaction zone was analyzed using EthoVision XT 11.5 (Noldus). The interaction zone was set at 7.39 cm around the pencil cup. The social interaction (SI) ratio was calculated by dividing the time spent in the interaction zone during the "target" session by the time spent in the same area during the "no target" session. Mice displaying an SI ratio equal to or greater than 1 were classified as "resilient", while those with a ratio less than 1 were classified as "susceptible".

Feeding test. A mouse previously provided with food *ad libitum* was transferred to a new cage with food pellets. The food left on a food hopper was collected and weighed at 4, 8, 12, and 16 hours after the beginning of the test.

Forced swim test. The test consisted of training and testing sessions conducted over two consecutive days. On the first day, a mouse expressing hM3Dq or control mCherry was placed in a glass beaker (12 cm diameter × 28 cm) filled with water (23 ± 1 °C) to 13 cm and forced to swim for 6 min for training. On the second day, the mice were treated with CNO (3 mg/kg) for 30 min and then forced to swim for another 6 min. Mouse behavior was recorded via video camera, and the last 4 min of the test was manually scored for immobility. Mice that made only slight movements necessary for body balancing or keeping their head out of the water were considered "immobile".

Social defeat stress models

Screening of aggressive CD-1 males. Retired male CD-1 breeders who initiated an attack on a C57BL/6 male intruder within <1 min were selected based on three consecutive resident intruder screening tests. CD-1 mice that exhibited <5 attack bouts within 5 min were used for the SSDS model. Those with >8 attack bouts within 5 min were used for the ASDS and CSDS models.

Subthreshold social defeat stress (SSDS) model. The SSDS model was developed as previously described (Supplementary Fig. 10a–f)[68,69]. A subject C57BL/6 male was introduced to an aggressive CD-1 male resident. After 5 to 10 min of attack encounters, the subject and aggressor were separated for 10 min by a perforated Plexiglas barrier in the middle of the cage. The subject mouse was then returned to its home cage and allowed to rest for 5 min. The whole session was repeated with another CD-1 aggressor. At the end of the second session, the subject mouse stayed in its home cage overnight. The social interaction, open field, and elevated plus maze tests were performed on the following 3 days. To assess the effects of SSDS on heart rate and blood corticosterone levels, we measured the heart rate of both unstressed and SSDS-treated mice one day before and one day after stress exposure, followed by blood collection.

Acute social defeat stress (ASDS) model. The ASDS model was developed following previous studies, with modifications (Supplementary Fig. 10g–k)[8,70]. A subject C57BL/6 male mouse was attacked successively by three CD-1 male aggressors for 3 to 4 min each and then returned to its home cage. After a 10-minute rest, the elevated plus maze, light-dark box, and open field tests were performed. On the following day, the mice were tested for social interaction with a novel CD-1 aggressor confined to a pencil cup. When astrocytic manipulation using hPMCA2w/b was necessary, an AAV expressing hPMCA2w/b or control mCherry was stereotaxically injected into the LS of the mice at the age of 5 weeks, and ASDS was applied 5 weeks after the viral injection.

Chronic social defeat stress (CSDS) model. CSDS was applied to C57BL/6 male mice, as previously described (Supplementary Fig. 10l–o)[66]. A mouse in the CSDS group was introduced to an aggressive CD-1 male resident. The subject was attacked for 5–10 min and then separated from the resident overnight by a perforated Plexiglas wall in the middle of the same cage. The whole session was repeated with different CD-1 aggressors for 10 consecutive days. A mouse in the control group was housed with a C57BL/6 male mouse for 24 h in separate cage compartments divided by a perforated Plexiglas barrier in the middle. The session was repeated for 10 consecutive days with different C57BL/6 males. Both control and socially defeated C57BL/6 mice were then subjected to behavioral tests for social interaction and anxiety during the following days.

c-Fos induction

To assess the influence of an increase in astrocytic Ca^{2+} on local neuronal excitation, a mouse expressing hM3Dq or control mCherry in LS astrocytes was injected with CNO (3 mg/kg) 90 min before being sacrificed for histological analysis. To examine the effect of the combined manipulation of LS astrocytes using hM3Dq and SSDS, an hM3Dq-expressing mouse was treated with CNO (3 mg/kg) 20 min before SSDS and then allowed to rest in a home cage for 50 min until perfusion. A control mouse was treated with CNO (3 mg/kg) and kept in a home cage for 120 min until perfusion.

Immunohistochemistry

A mouse was anesthetized by injecting 2% avertin (Acros Organics, 421430100) and perfused transcardially with 20 ml of PBS, followed by 20 ml of ice-cold 4% paraformaldehyde (Sigma-Aldrich, P6148) in PBS. The brain was dissected and cryoprotected in 30% sucrose for 24 to 48 h at 4 °C. The brain was then frozen in Optimum Cutting Temperature compound (Scigen, 4586) and stored at − 80 °C. Brain sections were cut at 30 µm on a cryostat (Leica, CM3050S). The sections were then treated with blocking solution (5% normal donkey serum in PBS containing 0.3% Triton X-100, NDST) for 1 h at room temperature and then incubated with primary antibodies diluted in 1% NDST at 4 °C overnight. The following day, the sections were rinsed with 0.3% Triton X-100 in PBS three times for 5 min each and then incubated with secondary antibodies diluted in 1% NDST for 2 h at room temperature. The primary antibodies used were rabbit anti-GFAP (1:500, Dako, Z0334), mouse anti-S100β (1:500, Novus Biologicals, NBP1-41373), rabbit anti-c-Fos (1:300, Cell Signaling, 2250), mouse anti-NeuN (1:500, Sigma-Aldrich, MAB377), and chicken anti-NeuN (1:500, Sigma-Aldrich, ABN91). The secondary antibodies used were Alexa 488-conjugated donkey anti-rabbit IgG (1:500, Thermo Fisher Scientific, A21206), Alexa 568-conjugated donkey anti-rabbit IgG (1:500, Thermo Fisher Scientific, A10042), Alexa 647-conjugated donkey anti-rabbit IgG (1:500, Thermo Fisher Scientific, A31573), Alexa 568-conjugated donkey anti-mouse IgG (1:500, Thermo Fisher Scientific, A10037), Alexa 647-conjugated donkey anti-mouse IgG (1:500, Thermo Fisher Scientific, A31571), Alexa 488-conjugated donkey anti-chicken IgY (1:500, Jackson ImmunoResearch, 703-545-155), and Alexa 647-conjugated donkey anti-chicken IgY (1:500, Jackson ImmunoResearch, 703-605-155). After the samples were embedded in a mounting medium (Vector Laboratories, Cat. No. ZH1122), the slides were dried overnight at room temperature in the dark before image acquisition. Fluorescence images were acquired using Axioscan.Z1 (Carl Zeiss) and confocal microscope (Carl Zeiss, LSM 700, LSM 800) and analyzed using ZEN 2.6 (Carl Zeiss) and Fiji (NIH) software. Immunofluorescence of GFAP and native fluorescence of mCherry were quantified using ZEN 2.6 (Carl Zeiss). Fluorescent cells were detected and counted using ImageJ (NIH). Manual correction by an experimenter blind to the treatments was applied to eliminate false-positive cells. The number of c-Fos^+ neurons or astrocytes ranged from 0.2 mm anterior to 0.2 mm posterior to the virus-infected LS regions.

To analyze the correlation between the number of c-Fos$^+$ cells and the fluorescence intensity of hM3Dq-mCherry, the target LS region was divided into 7 to 10 regions (147 μm × 147 μm). In each region, the average mCherry fluorescence was measured using ZEN 2.6 (Carl Zeiss), and the number of c-Fos$^+$ and NeuN$^+$ cells or c-Fos$^+$ and mCherry$^+$ cells was manually counted. The normalized mCh intensity was calculated by dividing each intensity value by the largest value in each group.

RNAscope in situ hybridization

The RNAscope multiplex fluorescent in situ hybridization was performed on fixed frozen tissue sections following the manufacturer's instructions (RNAscope Multiplex Fluorescent Reagent Kit v2; ACDBio, Cat. No. 323100). In brief, slides were dried for 1 hr at room temperature and were postfixed in 4% PFA for 15 min at 4 °C. Antigen retrieval was performed in 1X target retrieval reagent for 5 min at 90 °C, followed by treatment with RNAscope Protease III for 30 min. After incubation with probes, the slides were kept in 5X SSC (Invitrogen, Cat. No. 15-557-036) overnight at room temperature before proceeding to the amplification steps. Following the final wash, counterstaining was performed with DAPI (Thermo Fisher Scientific, Cat. No. 62248) at a concentration of 1:1000 in 1X PBS for 2 min. The following probes were used to detect gene expression: Mm-Fos-C1 (ACDBio, Cat. No. 316921-C1); Mm-Crhr2-C2 (ACDBio, Cat. No. 413201-C2); Mm-Nts-C2 (ACDBio, Cat. No. 420441-C2); and Mm-Gad1-C3 (ACDBio, Cat. No. 400951-C3). Fluorophores used to detect signals were as follows: TSA Vivid 650 (ACDBio, Cat. No. 323273) for the C1 probe; TSA Vivid 520 (ACDBio, Cat. No. 323271) for the C2 probes; and TSA Vivid 570 (ACDBio, Cat. No. 323272) for the C3 probe. Fluorophores were used at a concentration of 1:5000, except for sections probed with Mm-Crhr2-C2, where mCherry- and hM3Dq-expressing sections were stained at 1:3000 and 1:5000, respectively. After the samples were embedded in a mounting medium (Prolong Diamond Antifade Mountant; Invitrogen, Cat. No. P36970), the slides were dried overnight at room temperature in the dark before image acquisition was performed with a confocal microscope (Carl Zeiss, LSM 800). The co-localization of *c-Fos, Crhr2*, and *Nts* was identified and quantified using ImageJ (NIH). The percentage of overlap in *c-Fos*$^+$ cells, *Crhr2*$^+$, or *Nts*$^+$ cells was calculated exclusively in glutamic acid decarboxylase 1 (*Gad1*)$^+$ cells to exclude *c-Fos* induced in astrocytes.

Statistics

The data generated during this study is detailed in Supplementary Data 1. The data are expressed as the mean ± S.E.M (n = the number of animals or samples). The sample sizes provided in Supplementary Data 1 were determined by referencing those used in previously published papers. We analyzed all samples, excluding those in which virus expression or the position of the ferrule cannula deviated from the target. For fiber photometry and electrophysiology, all data were included in the analysis. The testing order for each group was determined randomly. Histological data were analyzed using paired or unpaired two-tailed t tests, two-way ANOVA with Bonferroni *post hoc* analysis, and Poisson regression. Fiber photometry results were analyzed using paired two-tailed t tests and two-way repeated-measures ANOVA with Bonferroni *post hoc* analysis. Blood corticosterone levels were analyzed using an unpaired two-tailed t test. Electrophysiological data were analyzed using two-way ANOVAs (data presented in Fig. 3) or repeated measures two-way ANOVAs (data presented in Fig. 4) with Bonferroni post hoc analyses. Behaviors were analyzed using a Mann–Whitney U test, two-way ANOVA with Bonferroni *post hoc* analysis, and Fisher's exact test using GraphPad Prism 7.0 (GraphPad Software Inc.). A p-value of less than 0.05 was considered significant.

Reporting summary

Further information on research design is available in the Nature Portfolio Reporting Summary linked to this article.

Data availability

All data supporting this study are included in the main text and supplementary files. Raw data are available upon reasonable request. Source data are provided in this paper.

Code availability

The MATLAB code used to process the fiber photometry data, along with demo datasets, is available on GitHub (https://doi.org/10.5281/zenodo.13917386).

References

1. O'Connor, D. B., Thayer, J. F. & Vedhara, K. Stress and health: A review of psychobiological processes. *Annu. Rev. Psychol.* **72**, 663–688 (2021).
2. Ménard, C., Hodes, G. E. & Russo, S. J. Pathogenesis of depression: Insights from human and rodent studies. *Neurosci.* **321**, 138–162 (2016).
3. Pitman, R. K. et al. Biological studies of post-traumatic stress disorder. *Nat. Rev. Neurosci.* **13**, 769–787 (2012).
4. De Kloet, E. R., Joëls, M. & Holsboer, F. Stress and the brain: from adaptation to disease. *Nat. Rev. Neurosci.* **6**, 463–475 (2005).
5. Sheehan, T. P., Chambers, R. A. & Russell, D. S. Regulation of affect by the lateral septum: implications for neuropsychiatry. *Brain Res. Rev.* **46**, 71–117 (2004).
6. Anthony, T. E. et al. Control of stress-induced persistent anxiety by an extra-amygdala septohypothalamic circuit. *Cell* **156**, 522–536 (2014).
7. Liu, Y. et al. A circuit from dorsal hippocampal CA3 to parvafox nucleus mediates chronic social defeat stress–induced deficits in preference for social novelty. *Sci. Adv.* **8**, eabe8828 (2022).
8. Jing, W. et al. A circuit of COCH neurons encodes social-stress-induced anxiety via MTF1 activation of Cacna1h. *Cell Rep.* **37**, 110177 (2021).
9. Besnard, A. et al. Dorsolateral septum somatostatin interneurons gate mobility to calibrate context-specific behavioral fear responses. *Nat. Neurosci.* **22**, 436–446 (2019).
10. Guzmán, Y. F. et al. Fear-enhancing effects of septal oxytocin receptors. *Nat. Neurosci.* **16**, 1185–1187 (2013).
11. Shin, S. et al. Drd3 signaling in the lateral septum mediates early life stress-induced social dysfunction. *Neuron* **97**, 195–208 (2018).
12. Carus-Cadavieco, M. et al. Gamma oscillations organize top-down signaling to hypothalamus and enable food seeking. *Nature* **542**, 232–236 (2017).
13. van der Veldt, S., Etter, G., Mosser, C. A., Manseau, F. & Williams, S. Conjunctive spatial and self-motion codes are topographically organized in the GABAergic cells of the lateral septum. *PLoS Biol.* **19**, e3001383 (2021).
14. Risold, P. Y. & Swanson, L. W. Chemoarchitecture of the rat lateral septal nucleus. *Brain Res. Rev.* **24**, 91–113 (1997).
15. Hashimoto, M. et al. Lateral septum modulates cortical state to tune responsivity to threat stimuli. *Cell Rep.* **41**, 111521 (2022).
16. Li, L. et al. Social trauma engages lateral septum circuitry to occlude social reward. *Nature* **613**, 696–703 (2023).
17. Azevedo, E. P. et al. A limbic circuit selectively links active escape to food suppression. *ELife* **9**, e58894 (2020).
18. Risold, P. Y. & Swanson, L. W. Connections of the rat lateral septal complex. *Brain Res. Rev.* **24**, 115–195 (1997).
19. Risold, P. Y. & Swanson, L. W. Structural evidence for functional domains in the rat hippocampus. *Science* **272**, 1484–1486 (1996).
20. Oh, S. W. et al. A mesoscale connectome of the mouse brain. *Nature* **508**, 207–214 (2014).
21. Wirtshafter, H. S. & Wilson, M. A. Lateral septum as a nexus for mood, motivation, and movement. *Neurosci. Biobehav. Rev.* **126**, 544–559 (2021).

22. Phelan, K. D., Hasuo, H., Twery, M. J. & Gallagher, J. P. Projection neurons in the rat dorsolateral septal nucleus possess recurrent axon collaterals. *Neurosci. Lett.* **97**, 259–265 (1989).
23. Staiger, J. F. & Nürnberger, F. The efferent connections of the lateral septal nucleus in the guinea pig: intrinsic connectivity of the septum and projections to other telencephalic areas. *Cell Tissue Res.* **264**, 415–426 (1991).
24. Leroy, F. et al. A circuit from hippocampal CA2 to lateral septum disinhibits social aggression. *Nature* **564**, 213–218 (2018).
25. Besnard, A. & Leroy, F. Top-down regulation of motivated behaviors via lateral septum sub-circuits. *Mol. Psychiatry* **27**, 3119–3128 (2022).
26. Liu, J.-J., Tsien, R. W. & Pang, Z. P. Hypothalamic melanin-concentrating hormone regulates hippocampus-dorsolateral septum activity. *Nat. Neurosci.* **25**, 61–71 (2022).
27. Li, H., Sung, H. H. & Lau, C. G. Activation of somatostatin-expressing neurons in the lateral septum improves stress-induced depressive-like behaviors in mice. *Pharmaceutics* **14**, 2253 (2022).
28. Wang, H. et al. Takeda G protein–coupled receptor 5 modulates depression-like behaviors via hippocampal CA3 pyramidal neurons afferent to dorsolateral septum. *Biol. Psychiatry* **89**, 1084–1095 (2021).
29. Allen, N. J. & Eroglu, C. Cell biology of astrocyte-synapse interactions. *Neuron* **96**, 697–708 (2017).
30. Panatier, A. et al. Astrocytes are endogenous regulators of basal transmission at central synapses. *Cell* **146**, 785–798 (2011).
31. Hwang, S. N., Lee, J. S., Seo, K. & Lee, H. Astrocytic regulation of neural circuits underlying behaviors. *Cells* **10**, 296 (2021).
32. Cui, Y. et al. Astroglial Kir4. 1 in the lateral habenula drives neuronal bursts in depression. *Nature* **554**, 323–327 (2018).
33. Wahis, J. et al. Astrocytes mediate the effect of oxytocin in the central amygdala on neuronal activity and affective states in rodents. *Nat. Neurosci.* **24**, 529–541 (2021).
34. Paxinos, G. & Franklin, K. B. *Paxinos and Franklin's the Mouse Brain in Stereotaxic Coordinates*. (Academic Press, 2019).
35. Eagle, A. L. et al. Circuit-specific hippocampal ΔFosB underlies resilience to stress-induced social avoidance. *Nat. Commun.* **11**, 4484 (2020).
36. Chen, Y. H. et al. Distinct projections from the infralimbic cortex exert opposing effects in modulating anxiety and fear. *J. Clin. Invest.* **131**, e145692 (2021).
37. Zheng, Z. et al. Hypothalamus-habenula potentiation encodes chronic stress experience and drives depression onset. *Neuron* **110**, 1400–1415 (2022).
38. Klapoetke, N. C. et al. Independent optical excitation of distinct neural populations. *Nat. Methods* **11**, 338–346 (2014).
39. Yang, L., Qi, Y. & Yang, Y. Astrocytes control food intake by inhibiting AGRP neuron activity via adenosine A1 receptors. *Cell Rep.* **11**, 798–807 (2015).
40. Kang, S. et al. Activation of astrocytes in the dorsomedial striatum facilitates transition from habitual to goal-directed reward-seeking behavior. *Biol. Psychiatry* **88**, 797–808 (2020).
41. Zhang, J.-m et al. ATP released by astrocytes mediates glutamatergic activity-dependent heterosynaptic suppression. *Neuron* **40**, 971–982 (2003).
42. Choi, I. S. et al. Astrocyte-derived adenosine excites sleep-promoting neurons in the ventrolateral preoptic nucleus: Astrocyte-neuron interactions in the regulation of sleep. *Glia* **70**, 1864–1885 (2022).
43. Yu, X. et al. Reducing astrocyte calcium signaling in vivo alters striatal microcircuits and causes repetitive behavior. *Neuron* **99**, 1170–1187 (2018).
44. Noh, K. et al. Cortical astrocytes modulate dominance behavior in male mice by regulating synaptic excitatory and inhibitory balance. *Nat. Neurosci.* **26**, 1541–1554 (2023).
45. Duncan, G. E., Knapp, D. J. & Breese, G. R. Neuroanatomical characterization of Fos induction in rat behavioral models of anxiety. *Brain Res.* **713**, 79–91 (1996).
46. An, M. et al. Lateral septum somatostatin neurons are activated by diverse stressors. *Exp. Neurobiol.* **31**, 376 (2022).
47. Besnard, A., Miller, S. M. & Sahay, A. Distinct dorsal and ventral hippocampal CA3 outputs govern contextual fear discrimination. *Cell Rep.* **30**, 2360–2373 (2020).
48. Gallagher, J. P., Zheng, F., Hasuo, H. & Shinnick-Gallagher, P. Activities of neurons within the rat dorsolateral septal nucleus (DLSN). *Prog. Neurobiol.* **45**, 373–395 (1995).
49. Chee, M. J., Arrigoni, E. & Maratos-Flier, E. Melanin-concentrating hormone neurons release glutamate for feedforward inhibition of the lateral septum. *J. Neurosci.* **35**, 3644–3651 (2015).
50. Wang, M. et al. Lateral septum adenosine A2A receptors control stress-induced depressive-like behaviors via signaling to the hypothalamus and habenula. *Nat. Commun.* **14**, 1880 (2023).
51. Oliveira, V. E. D. M. et al. Oxytocin and vasopressin within the ventral and dorsal lateral septum modulate aggression in female rats. *Nat. Commun.* **12**, 2900 (2021).
52. Dallérac, G., Zapata, J. & Rouach, N. Versatile control of synaptic circuits by astrocytes: where, when and how? *Nat. Rev. Neurosci.* **19**, 729–743 (2018).
53. Tan, Z. et al. Glia-derived ATP inversely regulates excitability of pyramidal and CCK-positive neurons. *Nat. Commun.* **8**, 13772 (2017).
54. Kelley, K. W. et al. Kir4.1-dependent astrocyte-fast motor neuron interactions are required for peak strength. *Neuron* **98**, 306–319 (2018).
55. Chung, W.-S. et al. Astrocytes mediate synapse elimination through MEGF10 and MERTK pathways. *Nature* **504**, 394–400 (2013).
56. Cavaccini, A., Durkee, C., Kofuji, P., Tonini, R. & Araque, A. Astrocyte signaling gates long-term depression at corticostriatal synapses of the direct pathway. *J. Neurosci.* **40**, 5757–5768 (2020).
57. Martin-Fernandez, M. et al. Synapse-specific astrocyte gating of amygdala-related behavior. *Nat. Neurosci.* **20**, 1540–1548 (2017).
58. Shindou, T. et al. Presynaptic adenosine A2A receptors enhance GABAergic synaptic transmission via a cyclic AMP dependent mechanism in the rat globus pallidus. *Br. J. Pharmacol.* **136**, 296–302 (2002).
59. Hasuo, H., Shoji, S., Gallagher, J. P. & Akasu, T. Adenosine inhibits the synaptic potentials in rat septal nucleus neurons mediated through pre-and postsynaptic A1-adenosine receptors. *Neurosci. Res.* **13**, 281–299 (1992).
60. Wang, M. et al. Genetic tagging of the adenosine A2A receptor reveals its heterogeneous expression in brain regions. *Front. Neuroanat.* **16**, 978641 (2022).
61. Gilpin, N. W., Herman, M. A. & Roberto, M. The central amygdala as an integrative hub for anxiety and alcohol use disorders. *Biol. Psychiatry* **77**, 859–869 (2015).
62. Fadok, J. P. et al. A competitive inhibitory circuit for selection of active and passive fear responses. *Nature* **542**, 96–100 (2017).
63. Babaev, O., Chatain, C. P. & Krueger-Burg, D. Inhibition in the amygdala anxiety circuitry. *Exp. Mol. Med.* **50**, 1–16 (2018).
64. Duvarci, S. & Pare, D. Amygdala microcircuits controlling learned fear. *Neuron* **82**, 966–980 (2014).
65. Lee, H. et al. Scalable control of mounting and attack by Esr1+ neurons in the ventromedial hypothalamus. *Nature* **509**, 627–632 (2014).
66. Golden, S. A., Covington, H. E. 3rd, Berton, O. & Russo, S. J. A standardized protocol for repeated social defeat stress in mice. *Nat. Protoc.* **6**, 1183–1191 (2011).
67. Berton, O. et al. Essential role of BDNF in the mesolimbic dopamine pathway in social defeat stress. *Science* **311**, 864–868 (2006).

68. Chaudhury, D. et al. Rapid regulation of depression-related behaviours by control of midbrain dopamine neurons. *Nature* **493**, 532–536 (2013).
69. Shen, C. J. et al. Cannabinoid CB1 receptors in the amygdalar cholecystokinin glutamatergic afferents to nucleus accumbens modulate depressive-like behavior. *Nat. Med.* **25**, 337–349 (2019).
70. Grossman, Y. S. et al. Structure and function differences in the prelimbic cortex to basolateral amygdala circuit mediate trait vulnerability in a novel model of acute social defeat stress in male mice. *Neuropsychopharmacol.* **47**, 788–799 (2022).

Acknowledgements

We thank J. Bang (Daegu Gyeongbuk Institute of Science and Technology, DGIST) and Dr. J.H. Kim (Kyungpook National University) for setting up experimental tools for astrocytes; J.S. Lee (DGIST), Dr. H.J. Jeon (Samsung Medical Center, Sungkyunkwan University), Dr. U. Kim (Hallym University), and Dr. S.J. Lee (Seoul National University, School of Dentistry) for feedback and discussions; J. Kim (DGIST and Korea Brain Research Institute) for help in setting up social defeat stress models; Dr. S.Y. Kim (Seoul National University) for help in setting up fiber photometric recordings and sharing mouse lines; Dr. Wookyung Yu (DGIST) for help in statistical analysis. This work was funded by the Basic Science Research Program funded through the National Research Foundation of Korea by the Ministry of Education, South Korea (RS-2024-00354104 and 2020R1A6A1A03040516 to H.L., 2020R1A2C3011464 to S.Y.C.) and the Korea Brain Research Institute Basic Research Program (21-BR-02-06 to H.L.).

Author contributions

K.S. and H.L. conceived and designed the project. K.S., S.W., H.Y.L., Y.S., S.L., H.P. and Y.G.K. performed the experiments. All authors discussed and interpreted the results. K.S., S.W., Y.S. and S.L. acquired and analyzed the fiber photometric, histological, and behavioral data. Y.G.K. and M.B. performed the RNAscope in situ hybridization, and K.S. and S.W. generated the brain sections and acquired and analyzed the images after the in situ hybridization. H.P., K.S. and D.J.K. acquired and analyzed the corticosterone data, and H.Y.L., K.S. and S.Y.C. acquired and analyzed the electrophysiological data. J.W.K. and K. Suk contributed to the establishment of the social defeat stress models and experimental tools for astrocytes, respectively. K.S., S.W., Y.S., H.Y.L., S.Y.Y. and H.L. prepared the figures. H.L. wrote the manuscript, with contributions from K.S., S.W., Y.S., H.Y.L., M.B. and S.Y.C. and supervised the project.

Competing interests

The authors declare no competing interests.

Additional information

Supplementary information The online version contains supplementary material available at https://doi.org/10.1038/s41467-024-54376-x.

Correspondence and requests for materials should be addressed to Se-Young Choi or Hyosang Lee.

Peer review information *Nature Communications* thanks Ciaran Murphy-Royal and the other anonymous reviewer(s) for their contribution to the peer review of this work. A peer review file is available.